DEPARTMENT OF

ATMOSPHERIC SCIENCES

UNIVERSITY OF WASHINGTON

SCIENTIFIC REPORT
on Contract NASA ~~NsG-632~~ NGR-48-002-009

PASSIVE MICROWAVE OBSERVATIONS OVER THE OCEANS

by

Lee U. Martin

August 1970

Prepared for
National Aeronautics and Space Administration
Goddard Space Flight Center
Greenbelt, Maryland

D E P A R T M E N T O F

A T M O S P H E R I C S C I E N C E S

UNIVERSITY OF WASHINGTON

SCIENTIFIC REPORT
on Contract NASA NsG-632

PASSIVE MICROWAVE OBSERVATIONS OVER THE OCEANS

by

Lee U. Martin

August 1970

Prepared for
National Aeronautics and Space Administration
Goddard Space Flight Center
Greenbelt, Maryland

PASSIVE MICROWAVE OBSERVATIONS OVER THE OCEANS

by

Lee U. Martin

A Master of Science thesis submitted to

THE DEPARTMENT OF ATMOSPHERIC SCIENCES
UNIVERSITY OF WASHINGTON

Supported by NASA Grant NsG-632, August 1970

PREFACE

Sea state changes are caused by weather factors such as wind, turbulence, fetch, lapse rate of the atmosphere and others. The sea state itself involves large waves, small capillary waves, white caps and foam. No world wide system to monitor sea state exists. The NASA observations of correlation of microwave emission with sea state opens a promising field of remotely sensing sea state. This thesis deals with the theoretical aspect of the problem and the detailed evaluation of numerous actual observational runs.

Konrad J. K. Buettner
Professor of Atmospheric Sciences
University of Washington

University of Washington

Abstract

PASSIVE MICROWAVE OBSERVATIONS

OVER THE OCEANS

by Lee Umphress Martin

Passive microwave observations offer a unique tool for obtaining information about our environment, particularly the ocean surface and the atmosphere above it. With the eventual use of microwave radiometers on satellites and the several hundred hours of observations already taken, there is a need for an analysis of the currently available data to determine the limits and capabilities of microwave observations under various oceanic and meteorological conditions.

This thesis investigates the predicted brightness temperatures that would be observed using several theoretical models of the ocean surface and atmosphere. Using these models, the predicted brightness temperatures are used to provide information about the following parameters: height of sensor, atmospheric effects, angular dependence of signal, surface roughness, surface films or slicks, foam and whitecaps.

Real atmospheric profiles of temperature and relative humidity are then used to calculate brightness temperatures for comparison to observed microwave observations over the oceans taken with a scanning radiometer at 19.35 GHz. Actual data used are from NASA Convair 990 flights over the Pacific Ocean, the Gulf of Mexico and the Salton Sea. As a result

of this investigation, conclusions are reached about the current theories of atmospheric and surface parameters and recommendations are made regarding possible modifications to the current roughness models of the ocean surface.

TABLE OF CONTENTS

LIST OF ILLUSTRATIONS

LIST OF TABLES

ACKNOWLEDGMENTS

I wish to express sincere thanks to Professor Konrad Buettner for his advice and guidance throughout the completion of this thesis.

To Professors Joost Businger and Donald Reynolds, who served on my reading committee, go special thanks for their helpful comments and consideration.

My special thanks to Dr. William T. Kreiss for his many stimulating discussions and the critical reading of the manuscript.

To my wife, Lynn, for her many sacrifices during this time and the careful drafting work, I owe my greatest thanks.

The research for this thesis has been primarily supported by the Goddard Space Flight Center of NASA under contract NsG-632 to the Department of Atmospheric Sciences, University of Washington. Other support came from the University of Washington Graduate School Research Fund, National Science Foundation Projects, under contract 11-0166.

CHAPTER 1

INTRODUCTION

The growing interest and need for information about our environment has led to the use of passive microwave observations to provide information about the character of the earth's surface and the atmosphere above it. Flight testing of these radiometers has taken place since the mid-sixties over a variety of terrain and under various atmospheric conditions. One of the most extensive programs has been that of NASA, using a single frequency radiometer operating at 19.35 GHz and employing an electrically scanning antenna with a 2.7° beamwidth. Over several hundred hours of data have been taken since May of 1967, with a preliminary analysis by (Catoe et al., 1967) and one on sea state measurements by (Nordberg et al., 1969). However, these analyses were based on scattered observations of a few specific cases. With modifications to theories being carried out and new data acquisitions being planned, there is a need for a more comprehensive analysis of the currently available data to determine how well the data agrees with the current theories of both surface and atmospheric parameters. From an analysis of the data, theoreticians can modify their theories to correspond to the data, or instruments can be modified to take advantage of the information obtained by an actual analysis of the data.

This thesis involves the analysis of NASA observations taken during 1967 over the Pacific Ocean and the Gulf of Mexico and during 1968 over the Salton Sea. These measurements were made from a variety of heights and under various surface and atmospheric conditions. Oceanic observations were chosen for study because they can provide information about the effect of roughness on the emissivity and reflectivity of a lossy medium and they allow information about the atmosphere to be determined, since over land measurements are swamped by the high emissivity of the land itself. Also, very few calculations have been made of the emissivity of various types of land surfaces compared to the relatively easy calculations which can be made for a smooth water surface.

Previous studies by Kreiss (1968) and Paris (1969) have considered various facets of the problem of remote sensing using passive microwave techniques. Based on their recommendations as to further study, this thesis was undertaken to include:

1. Numerous measurements under a variety of surface and atmospheric conditions.
2. Computations using real atmospheric profiles, if possible.
3. Angular dependence in the equations of radiative transfer.
4. Suitable emissivity laws at the air-sea boundary.

Thus, this thesis considers atmospheric emission and attenuation using a 14-layer model developed by Kreiss (1968), as part of his thesis. Modifications were made so that height variations of the sensor and viewing angles changes were incorporated. At first, model atmospheric profiles are considered to study the general effects, but actual radiosonde

data is used for comparison to actual observations. Basic models of the sea surface are then considered, including specular, diffuse and large scale roughness models. Using these surface models and various atmospheric profiles, the angular distribution of brightness temperatures are determined to see what results would be expected under various atmospheric and surface conditions. Then, using actual sea surface temperatures and radiosonde data, a comparison is made between actual observed measurements and those which would be expected. From these analyses, conclusions and recommendations are made regarding the measurement of atmospheric parameters and the modifications that are required in the current models which are used to describe scattering and emission from the sea surface.

CHAPTER 2

THEORY

This chapter provides an introduction into some of the factors involved in passive microwave observations of the ocean surface. Included are antenna parameters, atmospheric emission and attenuation and surface boundary conditions. Each of these factors will be considered in turn in order to provide a sufficient background for the discussion of theoretical brightness temperatures in Chapter 4 and the comparison between theoretical and observed data in Chapter 5.

2.1 Antenna Theory

A microwave radiometer is basically an ultrasensitive receiver which measures the total power received by an antenna. Measurements are usually made over a small frequency bandwidth, centered about a specific frequency and are of a specific polarization. Although the radiometer measures the power received, the output is usually given as antenna temperature, from which the "brightness temperature" can be recovered.

The power received by an antenna is given by Kraus (1966) as

$$w = \tfrac{1}{2} A_e \int_{\nu}^{\nu+\Delta\nu} \iint_{\Omega} B(\theta,\phi) P_n(\theta,\phi)\, d\Omega\, d\nu \qquad 2.1$$

where

w = received spectral power (watts/Hz)

A_e = effective area of the antenna (m^2)

$B(\theta,\phi)$ = intensity of distributed source (watts/m^2Hzster)

$P_n(\theta,\phi)$ = normalized power pattern of antenna

$d\Omega$ = element of solid angle ($\sin\theta d\theta d\phi$)

ν = frequency

The factor $\frac{1}{2}$ is introduced because the antenna receives only one polarization.

The directive gain of the antenna is expressed as,

$$D(\theta,\phi) = \frac{4\pi}{\lambda^2} A_e P_n(\theta,\phi) \qquad 2.2$$

and upon substituting 2.2 into 2.1, one obtains that

$$w = \frac{\lambda^2}{8\pi} \int_{\nu}^{\nu+\Delta\nu} \iint_{\Omega} B(\theta,\phi) D(\theta,\phi) d\Omega d\nu \qquad 2.3$$

If the source of radiation and the antenna pattern are uniform with respect to frequency over the bandwidth $\Delta\nu$, the total power becomes

$$w = \frac{\Delta\nu\lambda^2}{8\pi} \iint_{\Omega} B(\theta,\phi) D(\theta,\phi) d\Omega \qquad 2.4$$

The source of natural microwave radiation is the Planck black-body radiance given by

$$B_\nu = \frac{2h\nu^3}{c^2} \frac{1}{[e^{h\nu/kT}-1]} \quad \text{watts/m}^2\text{Hzster} \qquad 2.5$$

where

h = Planck's constant

ν = frequency

c = velocity of light in vacuum

k = Boltzman's constant

T = kinetic temperature

At microwave frequencies, $h\nu/kT \ll 1$, and one can simplify the source function by expanding the above term in brackets, yielding the Rayleigh-Jeans approximation, or

$$B = \frac{2k\nu^2 T}{c^2}, \quad \text{or} \quad \frac{2kT}{\lambda^2} \qquad 2.6$$

All natural radiation can be considered to be the combination of horizontal and vertical polarizations, where vertical polarization means that the electric vector lies in a plane containing both the direction of propagation and the vertical unit vector; horizontal polarization is in a plane perpendicular to that of vertical polarization. Thus, one can write,

$$B = B_h + B_v \qquad 2.7$$

Since the intensity and kinetic temperature are linearly related by equation 2.6, it is common to speak of "brightness temperature" instead of intensity. So by convention

$$B_p(\theta,\phi) = \frac{2kT_{bp}(\theta,\phi)}{\lambda^2} \qquad 2.8$$

where the subscript p will mean either horizontal or vertical polarization. Upon substitution of 2.8 into 2.4, we have

$$w = \frac{k\Delta\nu}{4\pi} \iint T_{bp}(\theta,\phi)D(\theta,\phi)d\Omega \qquad 2.9$$

For an impedance matched load at the receiver (no receiver noise power), the power absorbed by the antenna is

$$w = kT_a\Delta\nu \qquad 2.10$$

where

k = Boltzman's constant

T_a = antenna temperature

$\Delta\nu$ = frequency bandwidth

Upon substitution of 2.9 into 2.10, one can write that

$$T_a = \frac{1}{4\pi} \iint T_{bp}(\theta,\phi)D(\theta,\phi)d\Omega \qquad 2.11$$

where

$T_{bp}(\theta,\phi)$ = the total brightness temperature seen by the antenna

The total brightness temperature can be written as

$$T_{bp}(\theta,\phi) = \varepsilon_p(\theta,\phi)T_s(\theta,\phi) \qquad 2.12$$

where

$\varepsilon_p(\theta,\phi)$ = the polarized emissivity of the source

$T_s(\theta,\phi)$ = the kinetic temperature of the source

For black bodies, $\varepsilon_p = 1.0$. However, for most natural surfaces, $\varepsilon_p < 1.0$ and may be different for each polarization. In general, the emissivity of the surface will be a function of the frequency of observation, temperature, dielectric constant, roughness of the surface and the angle that the surface is viewed from.

For downward viewing observations from an aircraft or satellite, the total brightness temperature is the sum of three terms, as illustrated in Figure 2.1. They are

1. the emission from the earth's surface attenuated by the atmosphere
2. emission from the atmosphere between the earth's surface and the receiver, and
3. emission from the atmosphere reflected by the earth and attenuated by the atmosphere.

Thus, $T_{bp}(\theta,\phi)$ can be written as

$$T_{bp}(\theta,\phi) = [\varepsilon_p(\theta,\phi)T_s + r_p(\theta,\phi)T_{sky}(\theta,\phi)]\tau + \varepsilon_a T_{atms} \qquad 2.13$$

where

$\varepsilon_p(\theta,\phi)T_s$ = emission from the earth's surface

$r_p(\theta,\phi)T_{sky}(\theta,\phi)$ = sky contribution reflected by the earth

$\varepsilon_a T_{atms}$ = atmospheric contribution

τ = transmissivity of the atmosphere

(1) surface emission
(2) atmospheric emission
(3) reflected sky emission

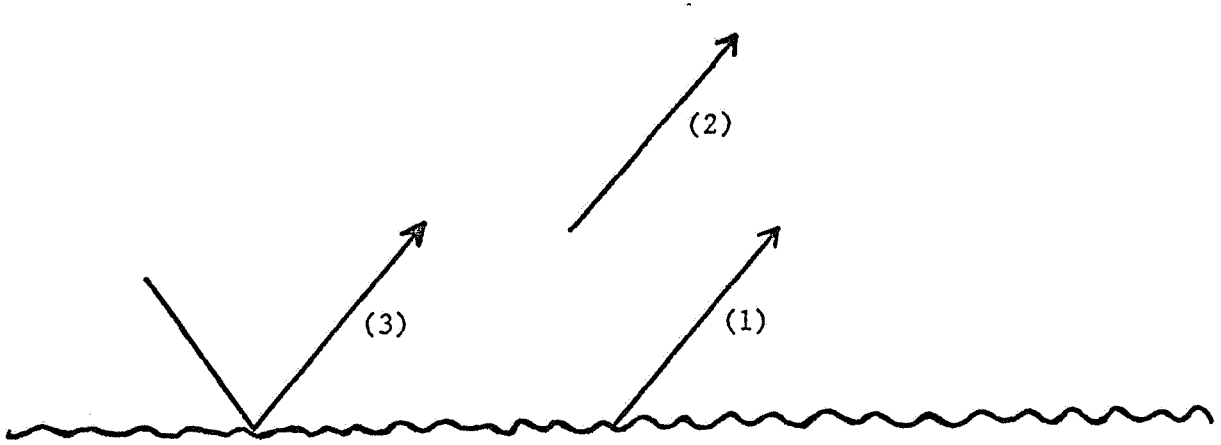

Fig. 2.1 Contributions to the total observed brightness temperature.

2.2 Radiative Equations

For radiation incident on a material, the conservation of energy requires that what is absorbed, reflected and transmitted must equal the total incident, or

$$a_\nu + r_\nu + \tau_\nu = 1 \qquad 2.14$$

where

a_ν = the absorptivity of the material

r_ν = the reflectivity of the material

τ_ν = the transmissivity of the material

Now Kirchhoff's law states that for bodies in local thermodynamic equilibrium, the absorptivity equals the emissivity, or

$$\varepsilon_\nu = a_\nu \qquad 2.15$$

where ε_ν = the emissivity of a material.

Using equations 2.15 and 2.16, we can consider several special cases which will be useful. For the atmosphere, if we neglect scattering ($r_\nu = 0$), which is a good assumption except in rain clouds, we have that

$$\varepsilon_\nu = 1 - \tau_\nu \qquad 2.16$$

And for the earth itself, where the transmissivity will equal zero, we find that

$$\varepsilon_\nu = 1 - r_\nu \qquad 2.17$$

These last two equations provide us with methods of determining the emissivity of the atmosphere and the earth's surface. Knowing the temperatures of these bodies and using the above equations, one can calculate the emission from these bodies and obtain the total brightness temperature. In the next section the effect of the atmosphere will be considered and following that, the earth's surface.

In the most general case, observations taken with a microwave radiometer involve both viewing angle and height variations of the sensor. This provides a much greater amount of useful information about both the surface characteristics and the atmosphere than those taken at a single height and viewing angle. Thus, the development which follows considers the solution to the two-dimensional equation of radiative transfer. Both oxygen and water vapor are considered as absorbing and emitting constituents in local thermodynamic equilibrium. A plane-parallel atmosphere is assumed and all scattering effects are neglected. The solution to the equations is due to Kreiss (1968) and allows for both easy understanding and numerical calculation.

2.3 Equation of Radiative Transfer

The equation of radiative transfer is a generalization of Schwarzchild's equation for two-dimensions and for two constituents. It can be written as

$$\mu \frac{dI_{\nu p}}{dz} = - \gamma_{\nu} (I_{\nu p} - S_{\nu p}) \qquad 2.18$$

where

$\mu = \cos\theta$ (zenith angle of observation)

$I_{\nu p}$ = monochromatic radiation intensity at height z

$S_{\nu p}$ = monochromatic source function at frequency ν and height z

γ_ν = absorption coefficient due to both oxygen and water vapor

Both oxygen and water vapor emit as black bodies and thus the source function is just equation 2.6, or

$$S_{p\nu} = \frac{2k\nu^2}{c^2} T_p \qquad 2.19$$

By applying the Rayleigh-Jeans approximation to the intensity, one can also write that

$$I_{\nu p} = \frac{2k\nu^2}{c^2} T_{bp} \qquad 2.20$$

And upon substituting equations 2.19 and 2.20 into equation 2.18, one obtains

$$\mu \frac{dT_b}{dz} = - \gamma_\nu (T_b - T) \qquad 2.21$$

This states that the incremental change in brightness temperature over the path length μdz is equal to the difference between the emission $\gamma_\nu T$ and the absorption $\gamma_\nu T_b$ along the path. From now on, the frequency dependence in the equations will be dropped for convenience.

2.4 Conversion to Pressure Coordinates

It is useful to convert the altitude increment to pressure units since the absorption coefficients of both oxygen and water vapor are pressure dependent. We can combine the equation of state

$$P = \rho_d RT \tag{2.22}$$

and the hydrostatic equation

$$\frac{dP}{dz} = - \rho_d g \tag{2.23}$$

where

P = atmospheric pressure (millibars)

ρ_d = density of dry air

R = atmospheric gas constant (see below)

g = mid-latitude acceleration of gravity

to form

$$dz = \frac{-RTdP}{g\ P} \tag{2.24}$$

Because of the variability of water vapor in the atmosphere, R is defined as

$$R = R_d\left[\frac{1 + \frac{w(p)}{\varepsilon}}{1 + w(p)}\right] \tag{2.25}$$

where

R_d = gas constant for dry air

$w(p)$ = mixing ratio

$\varepsilon = 0.622$

Upon substitution of equation 2.24 into 2.21, one obtains

$$\frac{\mu P g}{RT}\frac{dT_b}{dP} = -\gamma_\nu(T - T_b) \qquad 2.26$$

2.5 Solution to the Equation of Radiative Transfer

Kreiss assumed that there exists an average temperature $\bar{T}_i$ for each atmospheric layer which represents the mean radiating temperature of that layer. Thus, equation 2.26 can be written as

$$\frac{dT_b}{\bar{T}_i - T_b} = -\frac{R\bar{T}_i}{\mu g}\gamma_\nu(P,\bar{T}_i)\frac{dP}{P} \qquad 2.27$$

This equation can be integrated over a layer of finite thickness to yield

$$\int_{T_{bi}}^{T_{bi+1}} \frac{dT_b}{\bar{T}_i - T_b} = -\int_{P_i}^{P_{i+1}} \frac{R\bar{T}_i}{\mu g}\gamma_\nu(P,\bar{T}_i)\frac{dP}{P} \qquad 2.28$$

The left side becomes

$$\ln\frac{\bar{T}_i - T_{bi+1}}{\bar{T}_i - T_{bi}} \qquad 2.29$$

and upon raising both sides to the base of the natural logarithm, the equation can be written as

$$\frac{\bar{T}_i - T_{bi+1}}{\bar{T}_i - T_{bi}} = \exp\left[\frac{-\sec\theta R\bar{T}_i}{g}\int_{P_i}^{P_{i+1}}\gamma_\nu(P,\bar{T}_i)\frac{dP}{P}\right] \qquad 2.30$$

The right side of equation 2.30 is just the form of a transmissivity τ, where

$$\tau = \exp[-\sec\theta \int_0^z \alpha(z)dz] \qquad 2.31$$

Thus, for each atmospheric layer, one can write that

$$T_{bi+1} = (1 - t_i)\bar{T}_i + T_{bi}t_i \qquad 2.32$$

Equation 2.16 stated that for the atmosphere, $\varepsilon = 1 - \tau$. Equation 2.32 says that the temperature at the top of the layer is the sum of the emissivity of the layer times its temperature, plus the flux incident on the bottom of the layer times the transmissivity of the layer. Knowing the contribution from each layer, the total effect of the atmosphere can be obtained by using equation 2.32 and having the flux emerging from one layer becoming the flux incident on the above layer. Thus, the atmospheric contribution looking upwards can be written as

$$T_b^{(up)} = (1-t_1)\bar{T}_1 + (1-t_2)\bar{T}_2t_1 + (1-t_3)\bar{T}_3t_1t_2 + (1-t_{n-1})\bar{T}_{n-1}t_1 \text{ ----- } t_{n-1} \qquad 2.33$$

and that looking downward as

$$T_b^{(down)} = (1-t_1)\bar{T}_1t_2 \text{ ----- } t_{n-1} + (1-t_2)\bar{T}_2t_3 \text{ ----- } t_{n-1} + (1-t_{n-1})\bar{T}_{n-1} \qquad 2.34$$

2.6 Absorption Coefficients

For ease in numerical calculation, the righthand side of equation 2.30 can be written as follows

$$\exp[-\sec\theta(\frac{R\bar{T}_i}{g}\int_{P_i}^{P_{i+1}}\alpha_\nu^{(o)}\frac{dP}{P}+\frac{R\bar{T}_i}{g}\int_{P_i}^{P_{i+1}}\alpha_\nu^{(v)}\ (P_i,\bar{T}_i)\frac{dP}{P})] \qquad 2.35$$

where

$\alpha_\nu^{(o)}$ = absorption coefficient for oxygen

$\alpha_\nu^{(v)}$ = absorption coefficient for water vapor

These integrals are given below and their functional form will be found in Chapter 3 in the computer program.

$$\frac{R\bar{T}_i}{g}\int_{P_i}^{P_{i+1}}\alpha_\nu^{(o)}\frac{dP}{P}=\frac{c_1R_d\nu^2}{gT_i^2}\sum_N e^{\frac{-EN}{k\bar{T}_i}}f_n(\nu,\beta_i,P_i,P_{i+1},T_i) \qquad 2.36$$

$$\frac{R\bar{T}_i}{g}\int_{P_i}^{P_{i+1}}\alpha_\nu^{(v)}\frac{dP}{P}=\frac{R_i\bar{T}_i}{g}\alpha_\nu^{(v)}\ (P_i,\bar{T}_i)\ \ln\frac{P_{i+1}}{P_i} \qquad 2.37$$

2.7 Surface Boundary Conditions

The development to follow is based on the work of Peake (1969), since his analysis considers all types of surfaces, with specular and Lambertian (diffuse) being special cases. Ultimately, the brightness temperature observed by a radiometer is determined by the dielectric constant, the temperature and the roughness of the surface. However, as seen in the previous development, these characteristics of the surface are usually given in terms of derived parameters, either the emissivity or the reflectivity. These in turn can be described in terms of the differential scattering cross-section.

Consider Figure 2.2, which shows the scattering geometry, and consider a plane wave of intensity I_o(watts/m^2) and polarization state j incident on a small section of terrain A. The intensity I_s scattered by the surface in the direction (θ_s,ϕ_s) with polarization state k at a distance R is given by

$$4\pi R^2 I_s = \sigma_{jk}(0,s) I_o A \tag{2.38}$$

where

$\sigma_{jk}(0,s)$ = differential scattering cross-section per unit area of terrain

j = state of incident polarization

k = state of scattered polarization

$\theta_o\phi_o$ = direction of incident wave

$\theta_s\phi_s$ = direction of scattered wave

By the Lorentz reciprocity condition

$$\sigma_{jk}(0,s) = \sigma_{kj}(s,0) \tag{2.39}$$

The albedo is defined as the ratio of the power incident on the surface from the direction (θ_o,ϕ_o), at a specific polarization and frequency, to that which is scattered. With this definition, the albedo becomes

$$A_i(\theta_o,\phi_o) = \frac{\sec\theta_o}{4\pi} \iint_{\Omega} (\sigma_{jk} + \sigma_{jj}) d\Omega \tag{2.40}$$

where the integration is taken over by the upper hemisphere and the total scattered power includes both polarizations.

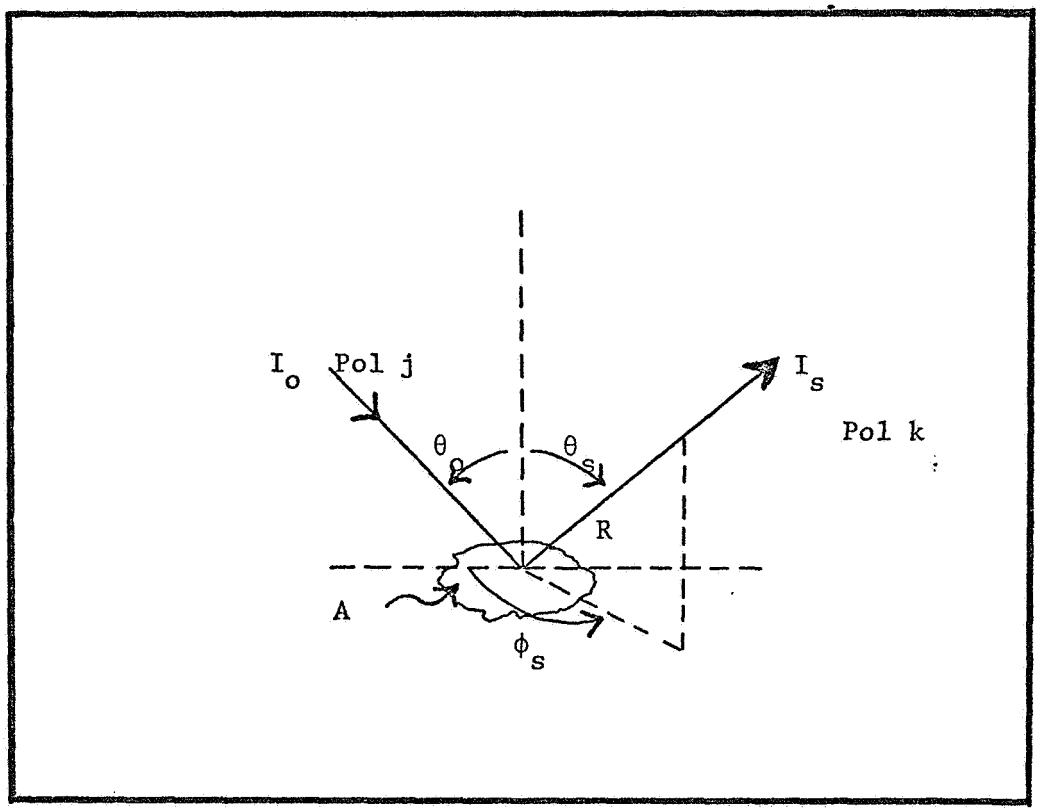

Fig. 2.2 Scattering geometry(after Peake, 1969).

Since what is not scattered is absorbed, the absorption coefficient becomes

$$a_j(\theta_o,\phi_o) = 1 - A_j(\theta_o,\phi_o) = 1 - \frac{\sec\theta_o}{4\pi} \iint_{\Omega} (\sigma_{jk}+\sigma_{jj})d\Omega \qquad 2.41$$

and by the principle of detailed balance, the emissivity equals the absorption, or

$$\varepsilon_j(\theta_o,\phi_o) = a_j(\theta_o,\phi_o) \qquad 2.42$$

These equations are the most general form of Kirchhoff's law, taking account of both the polarization and the angular dependence of the coefficients. From them, the emissivity of a material can be determined from the differential scattering cross-section.

From the derivations above, the emission from the surface can be written as

$$\varepsilon_s(\theta,\phi)T_s = [1 - \frac{\sec\theta_o}{4\pi} \iint_{\Omega} (\sigma_{jk}+\sigma_{jj})d\Omega]T_s \qquad 2.43$$

and the reflected sky term is written as

$$r_s(\theta,\phi)T_{sky}(\theta,\phi) = \frac{\sec\theta_o}{4\pi} \iint_{\Omega} T_{sky}(\theta,\phi)(\sigma_{jk}+\sigma_{jj})d\Omega_s \qquad 2.44$$

To evaluate these terms, the form of the differential scattering coefficients must be determined. For relatively simple surfaces, their form is well known and the integrals can be evaluated easily. For most natural surfaces, however, empirical laws are assumed and the coefficients

are determined from experiment. I will consider several surface models in turn which can represent the scattering from the sea surface under various conditions.

2.8 Specular Surfaces

For a perfectly smooth surface, the differential scattering cross-section has the form of a delta function, and is given by

$$\sigma_{jk}(0,s) = 4\pi|R_p|^2 \cos\theta_{sp} \csc\theta_{sp}\delta(\theta_s-\theta_{sp})\delta(\phi_s-\phi_{sp}) \qquad 2.45$$

where θ_{sp} and ϕ_{sp} represent the specular direction and $|R_p|^2$ is the reflection coefficient for either horizontal or vertical polarization. Upon substitution into equation 2.43, the surface emission becomes

$$\varepsilon_s(\theta,\phi)T_s = [1 - \int_0^{2\pi}\int_0^{\pi/2} |R_p|^2\delta(\theta_s-\theta_{sp})\delta(\phi_s-\phi_{sp})d\theta d\phi]T_s \qquad 2.46$$

which reduces to

$$\varepsilon_s(\theta,\phi)T_s = [1 - |R_p|^2]T_s \qquad 2.47$$

The reflected sky contribution becomes (equation 2.44)

$$r_s(\theta,\phi)T_{sky}(\theta,\phi) = \int_0^{2\pi}\int_0^{\pi/2} |R_p|^2 T_{sky}(\theta,\phi)\delta(\theta_s-\theta_{sp})\delta(\phi_s-\phi_{sp})d\theta d\phi \qquad 2.48$$

which reduces to

$$r_s(\theta,\phi)T_{sky}(\theta,\phi) = |R_p|^2 T_{sky}(\theta,\phi) \qquad 2.49$$

The reflection coefficients are just the Fresnel coefficients for horizontal and vertical polarization and can be put into the following form for easy calculation (Sirounian, 1969).

$$|R_h|^2 = \frac{[(p-\mu)^2 + q^2]}{[(p+\mu)^2 + q^2]} \qquad 2.50$$

$$|R_v|^2 = \frac{[(\mu e'-p)^2 + (\mu e''-q^2)]}{[(\mu e'+p)^2 + (\mu e''+q^2)]} \qquad 2.51$$

where

e' = the real part of the complex dielectric constant of water

e'' = the imaginary part of the dielectric constant of water

$\mu = \cos\theta$, where θ is the angle of incidence of observation

p and q are given as follows

$$p = \frac{1}{\sqrt{2}} \{[(e'+\mu^2-1)^2 + e''^2]^{\frac{1}{2}} + (e'+\mu^2-1)\}^{\frac{1}{2}} \qquad 2.52$$

$$q = \frac{1}{\sqrt{2}} \{[(e'+\mu^2-1)^2 + e''^2]^{\frac{1}{2}} - (e'+\mu^2-1)\}^{\frac{1}{2}} \qquad 2.53$$

Various authors (Sirounian, Stogryn, Kreiss and Paris) have used slightly different values for e' and e'', based upon the work of Lane and Saxton (1952). The primary difference between the authors is the relaxation time of the water molecule, which will vary with the salinity of the water. Since there was this difference, a comparison was made between their results to determine what the actual differences would be. This

is essential since the emission from the ocean at 19.35 GHz amounts to 85 to 90 percent of the total brightness temperature received at nadir viewing angles and differences in emissivity of 0.01 will contribute differences of about 3°K, depending on the water temperature.

Values of e' and e'', as a function of the water temperature, calculated from data used by each of the authors, are shown in Figures 2.3 and 2.4. It can be seen that the differences between authors are significant. In my calculations shown below, the values obtained by Paris (1969) have been used, and the salinity was assumed to equal $35°/_{oo}$. Figure 2.5 shows the angular variation of reflectivity for both horizontal and vertical polarizations for two extremes of temperature. Figure 2.6 gives the corresponding emissivity values. Values for other temperatures will lie between these extremes and are given in Table 2.1. Table 2.2 shows the surface contribution to the total brightness temperature for nadir viewing as a function of the surface temperature and neglecting atmospheric effects. It can be seen that there would be ambiguity in measurements made at 19.35 GHz without knowing something beforehand about the surface temperature. However, the maximum difference would only amount to 2°K for a range of surface temperatures of 30°K.

2.9 Diffuse Surface

Although there are various models of diffuse surfaces which are being used to explain scattering measurements, I will use a Lambertian surface. This model will provide the opposite case to that of a specular surface and should provide the upper limit to scattering from the sea

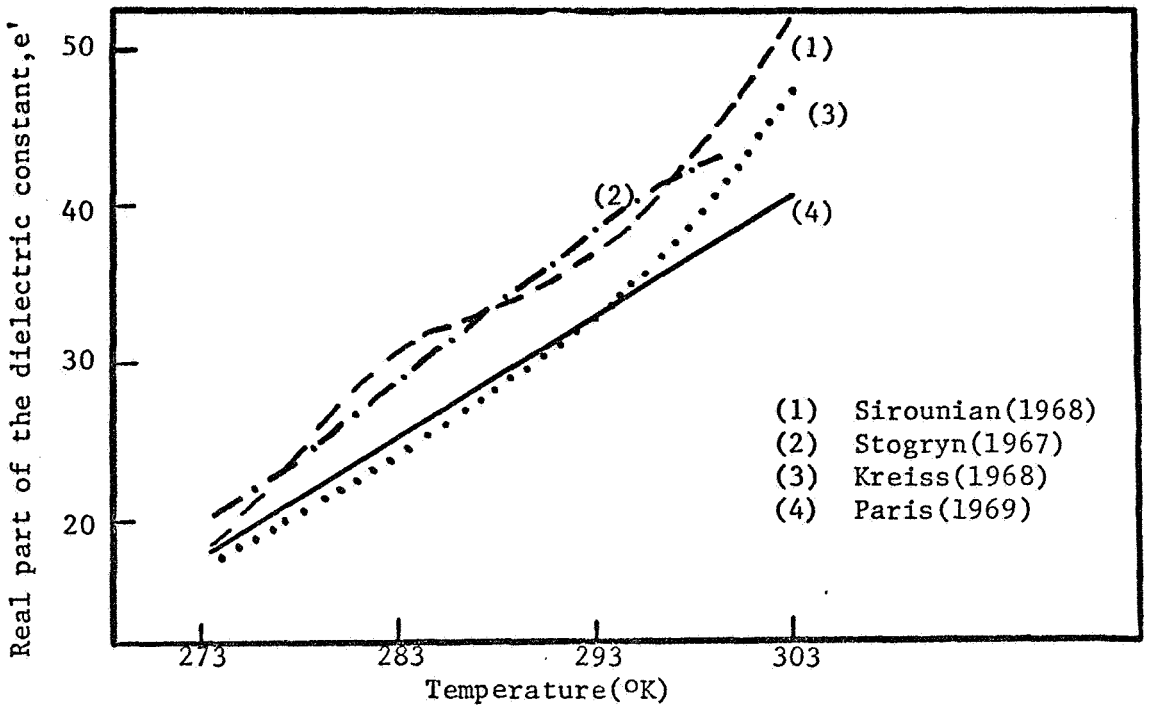

Fig. 2.3 Variation of real part of dielectric constant of water with temperature.

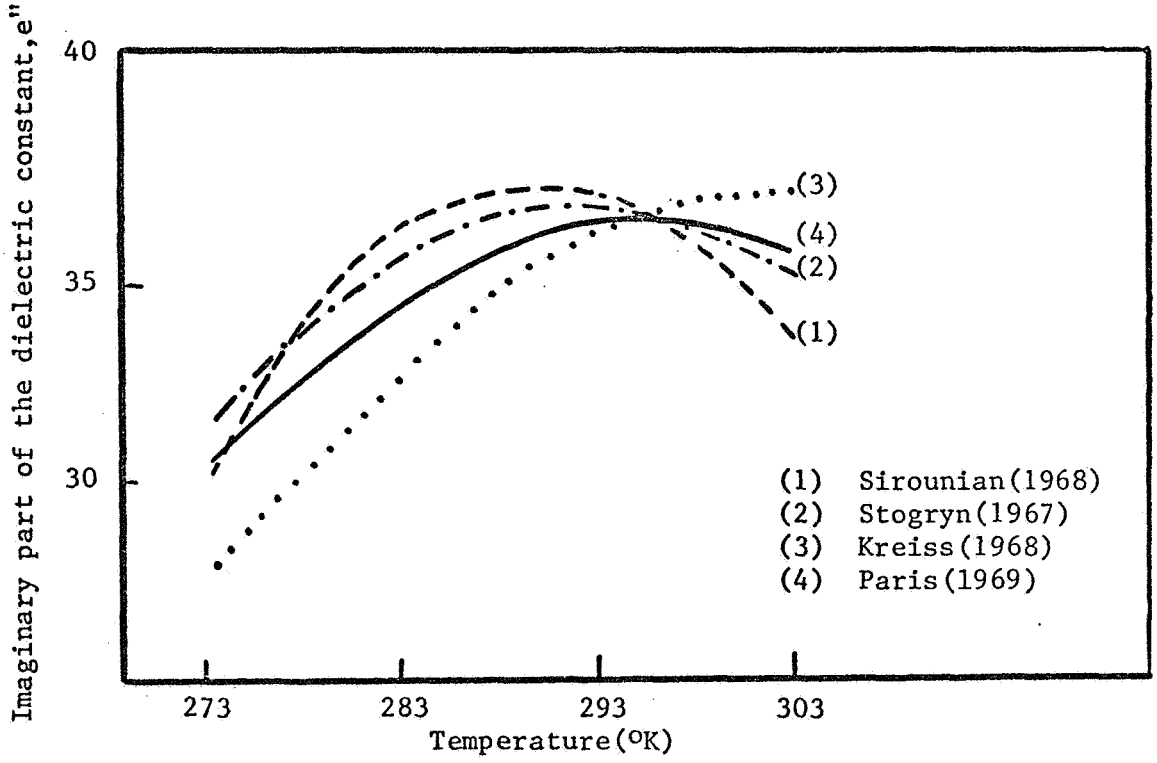

Fig. 2.4 Variation of imaginary part of dielectric constant of water with temperature.

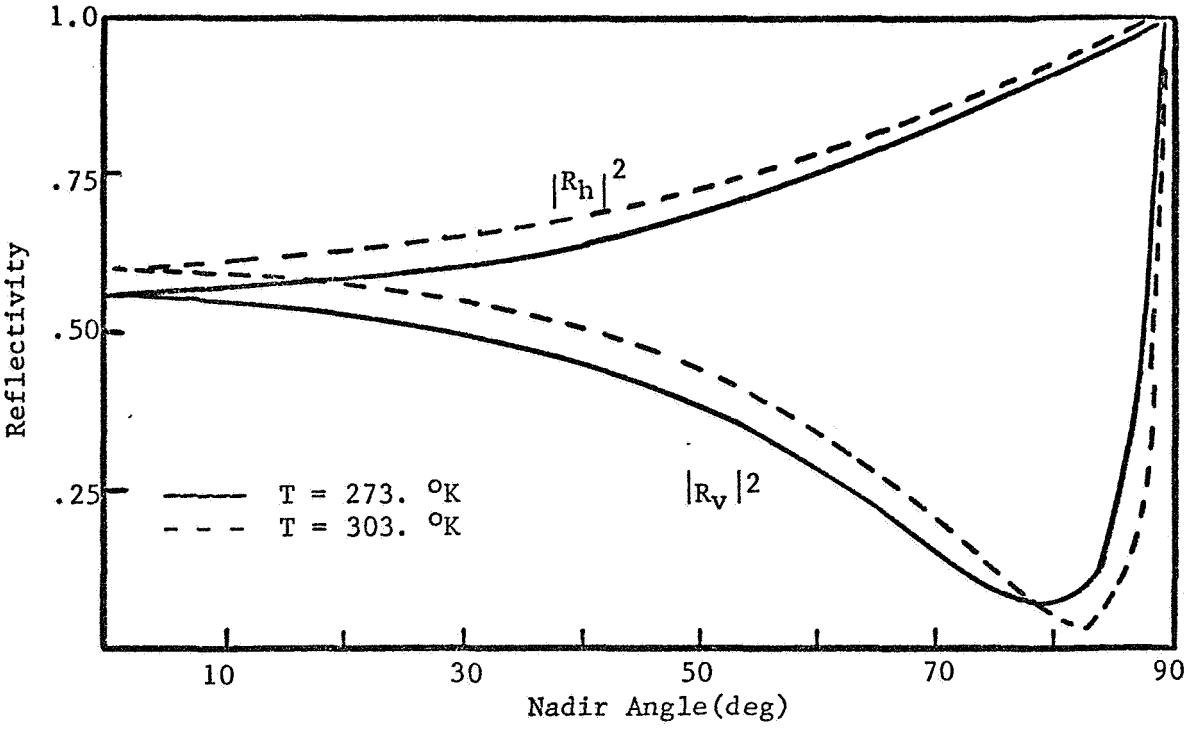

Fig. 2.5 Angular variation of reflectivity for smooth water surface and both polarizations.

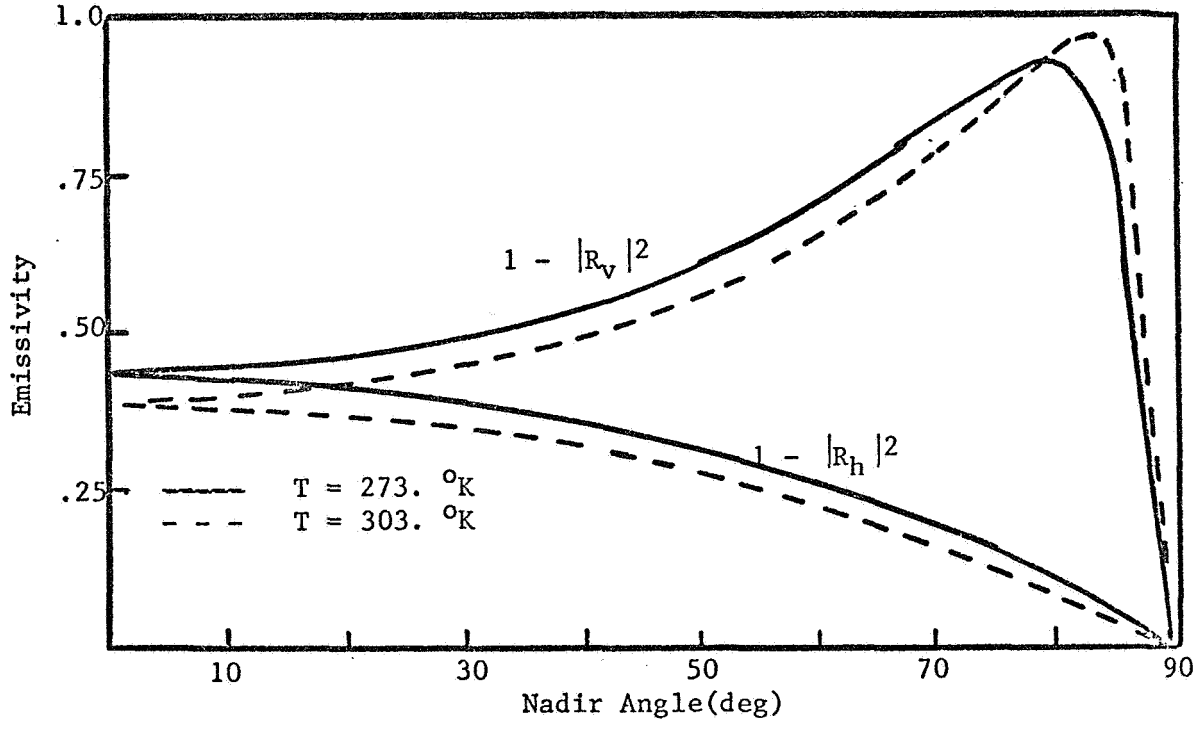

Fig. 2.6 Angular variation of emissivity for smooth water surface and both polarizations.

Table 2.1 Reflectivity for smooth water surface (horizontal polarization)

	Surface temperature (K)				
Angle (deg)	278.	283.	288.	293.	298.
0	.5759	.5860	.5939	.6003	.6046
10	.5807	.5908	.5986	.6049	.6092
20	.5953	.6052	.6128	.6190	.6231
30	.6200	.6294	.6367	.6426	.6466
40	.6551	.6639	.6707	.6762	.6799
50	.7011	.7091	.7152	.7200	.7233
60	.7586	.7653	.7704	.7745	.7772
70	.8277	.8327	.8365	.8395	.8416
80	.9084	.9112	.9133	.9149	.9161
90	1.0000	1.0000	1.0000	1.0000	1.0000

Table 2.2 Surface contribution at Nadir

Sfc. Temp. (°K)	$\varepsilon_s T_s$
273.0	119.0
278.0	117.5
283.0	117.0
288.0	117.0
293.0	117.0
298.0	117.8
303.0	119.0

surface (in the absence of foam, multiple reflections and shadowing effects). The differential scattering cross-section for this surface is given as, Peake (1969)

$$\sigma(0,s) = \Gamma\cos\theta_o\cos\theta_s \qquad 2.54$$

where Γ is only a function of the frequency of observation. For a perfectly diffuse surface, we have no information about polarization, so that

$$\sigma(0,s) = \sigma_{jk}(0,s) + \sigma_{jj}(0,s) \qquad 2.55$$

Upon substitution into equation 2.43, the surface emission becomes

$$\varepsilon_s(\theta,\phi)T_s = [1 - \frac{\Gamma}{4\pi}\iint_{\Omega} \cos\theta_s d\Omega]T_s \qquad 2.56$$

which reduces to

$$\varepsilon_s(\theta,\phi)T_s = (1 - \frac{\Gamma}{4})T_s \qquad 2.57$$

The reflected sky term (equation 2.44) is

$$r_s(\theta,\phi)T_{sky}(\theta,\phi) = \frac{\Gamma}{4\pi}\iint_{\Omega} T_{sky}(\theta,\phi)\cos\theta d\Omega \qquad 2.58$$

Now, the problem arises as to how to evaluate Γ. The usual method is to evaluate Γ from backscattering measurements. A method that doesn't rely on experimental results is to assume that the hemispherical albedo

should be the same for all types of surfaces, if one neglects shadowing and multiple reflections. Thus, the total amount of reflected energy should be the same, only the angular distribution of this energy will be different. Since the albedo for a diffuse surface equals $\Gamma/4$, we can equate the reflection from the diffuse surface to that of a specular surface and write

$$\iint_{\Omega} \frac{\Gamma}{4} \cos\theta d\Omega_s = \tfrac{1}{2} \iint_{\Omega} |R_h|^2 \cos\theta d\Omega_s + \tfrac{1}{2} \iint_{\Omega} |R_v|^2 \cos\theta d\Omega_s \qquad 2.59$$

where the reflected energy from a diffuse surface is one-half the sum of the vertical and horizontal polarizations because it contains both components. This calculation has been done using the equations in the previous section for the values of $|R_h|^2$ and $|R_v|^2$. These values are given in Table 2.3 for various temperatures of the water surface.

Table 2.3 Values of $\Gamma/4$ versus temperature

Sfc Temp.	$\Gamma/4$
273.0	0.5399
278.0	0.5499
283.0	0.5588
288.0	0.5656
293.0	0.5710
298.0	0.5745
303.0	0.5766

Since we will assume azimuthal symmetry for all our calculations, equation 2.58 reduces to the following

$$r_s(\theta,\phi)T_{sky}(\theta,\phi) = \frac{\Gamma}{2}\int_0^{\pi/2} T_{sky}(\theta)\cos\theta d\theta \qquad 2.60$$

2.10 Stogryn's Roughness Model

Stogryn (1967), using Peake's definitions of the scattering coefficients, derived expressions for the scattering from rough, finitely conducting surfaces based on the Kirchhoff approximation; that is, the fields on the surface are calculated locally as if the surface were plane. The roughness of the surface was normally distributed and is given in terms of the root mean square slopes of the surface, g_x and g_y. Slope measurements for the oceans were based on measurements made by Cox and Munk (1954a and 1954b), and are given by the following expressions

$$g_x^2 = 0.003 + 1.92 \times 10^{-3}\, w \qquad 2.61$$

$$g_y^2 = 3.16 \times 10^{-3}\, w \qquad 2.62$$

where w is the wind speed at a height of 41 feet in m/sec. Stogryn's expression for the scattering coefficients are of the following form

$$\gamma_{ab}(\underset{\sim}{\hat{k}}_o,\underset{\sim}{\hat{k}}) = \frac{f_{ab}\,\exp\left[-\frac{1}{2B^2}(\alpha^2/g_x^2 + \beta^2/g_y^2)\right]}{2\cos\theta_o B^2 g_x g_y} \qquad 2.63$$

2.63

where

f_{ab} = a function of the angles of incidence and reflection and the reflection coefficients

α,β,B = functions of the scattering geometry

Stogryn did not provide curves for the emissivity of the surface based on the above coefficients, so one cannot compare how they vary with angle as compared to the emissivity of a specular or diffuse surface. However, Figure 2.7 shows the total brightness temperature received using this model for the following conditions: 1) a surface temperature of 290.°K; 2) a standard atmosphere; 3) observer height of 1 km; 4) a frequency of 19.4 GHz; 5) horizontal polarization, and 6) wind speeds from 4 to 14 m/sec. There is little difference between the curves of various surface roughness at close to nadir viewing angles, but increasing temperature differences at large viewing angles. For the roughest case considered, the curve approaches almost uniform brightness temperature with angle. This is similar in angular dependence to that expected from a diffuse surface, as will be seen in Chapter 4.

2.11 Foam and Whitecaps

Recent measurements of downward viewing radiometric observations from aircraft (Nordberg et al., 1969) led to the speculation that the unusually high brightness temperatures observed were due to the presence of foam and whitecaps on the ocean surface. The fact that foam could cause large temperature increases was confirmed by Williams (1969), using land-based measurements of soap bubbles. Although Williams' measurements confirmed the high emissivity of foam, no absolute data were obtained because his observations were made in the near field of the radiometers. More recent measurements by Nordberg et al. during 1969 over the Irish Sea have provided additional evidence that foam can have

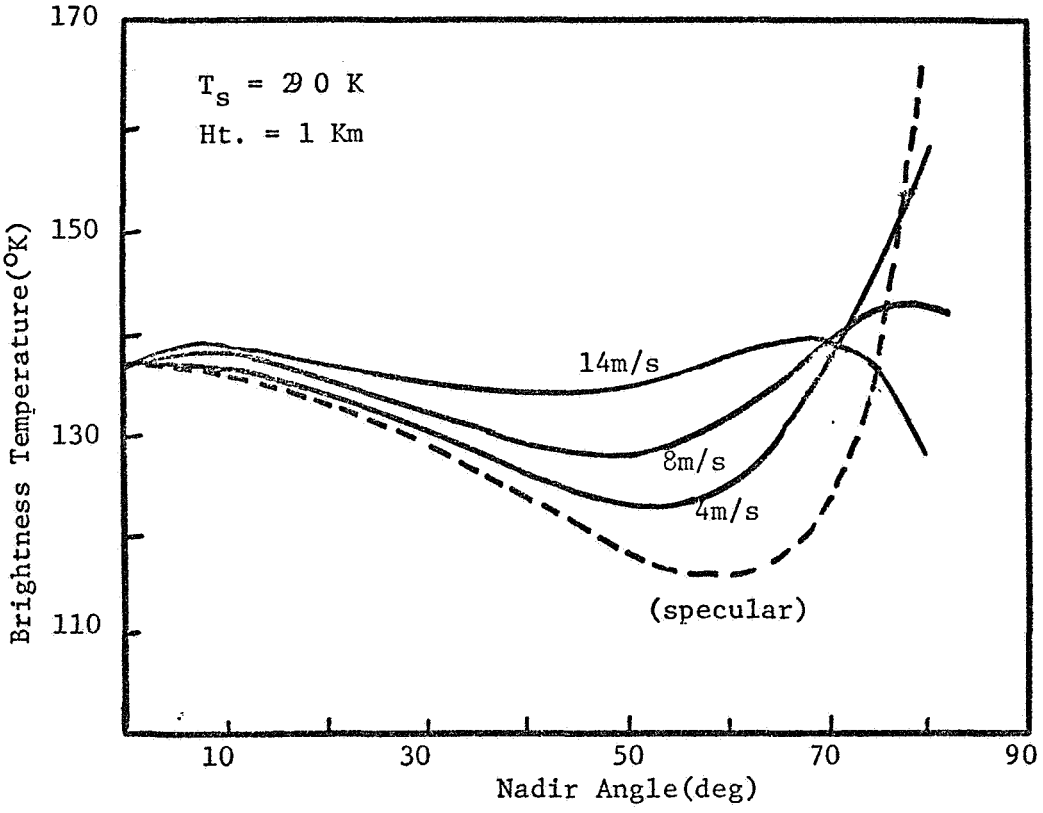

Fig. 2.7 Angular variation of brightness temperature for rough surface model(after Stogryn,1967).

high emissivity values. Measurements were made at low altitudes (500 feet), so that the antenna beam was completely filled by a foam patch. The resulting brightness temperatures observed were close to the thermodynamic temperature of the water, indicating that the emissivity of the foam was close to 1.0. Thus, there is little doubt that foam may have a much higher value of emissivity than a plane water surface. This section will provide an introduction into some of the properties of foam, including some of the factors involved in its formation, stability, dielectric constant and amount formed.

The primary cause of foam formation is the breaking of waves on the water surface, although the decomposition of organic matter and the impact of raindrops can be important. In general, the amount of foam actually produced will depend on the character of the water surface, the salinity of the water and the atmospheric stability. Each of these factors will be considered in turn.

The character of the ocean surface plays an important role in that the number of breaking waves will, in general, be different for the same surface wind speed. This difference can be caused by proximity to land, the height and direction of swell, the duration of the wind and the fetch over which the wind has been blowing. Rarely will these conditions be similar enough to say that the number of breaking waves will be the same.

The effect of salinity on the foaming ability of sea water was studied by Miyake and Abe (1948), and their results are shown in Figure 2.8. Increasing salinity increases the amount of foaming ability, reaching a maximum at a definite concentration. From this data, Miyake and

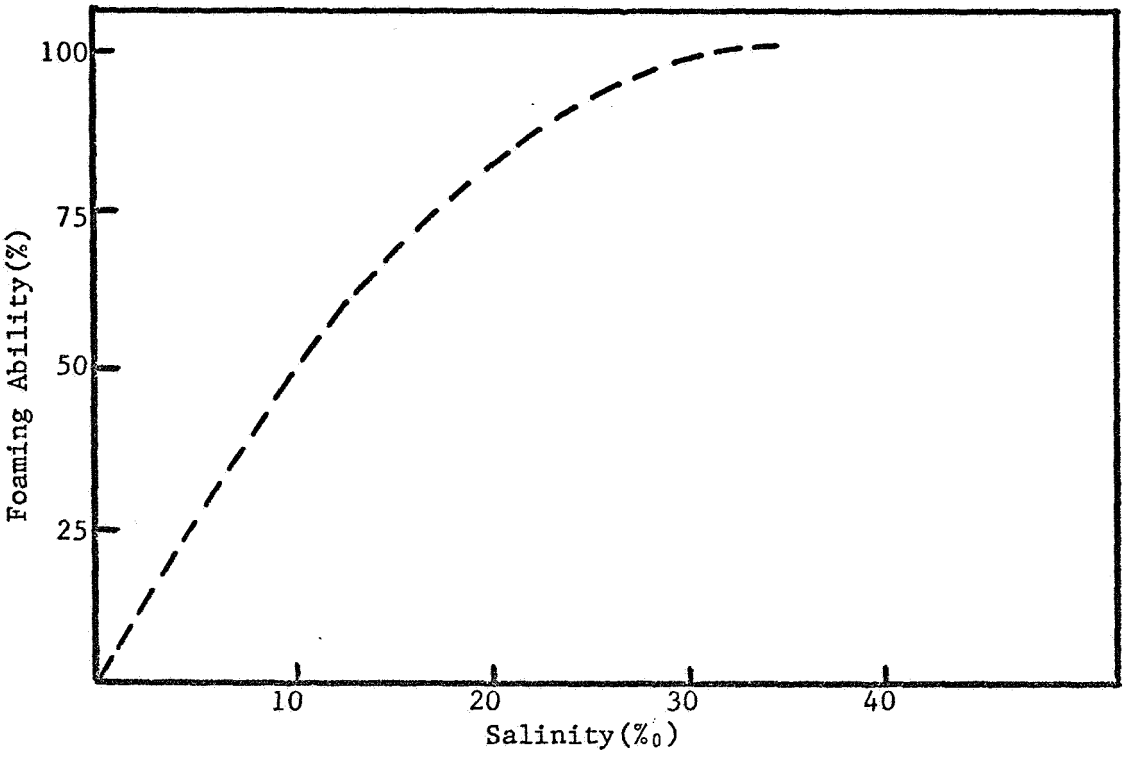

Fig. 2.8 Effect of salinity on the foaming ability of sea water(after Miyake & Abe,1948).

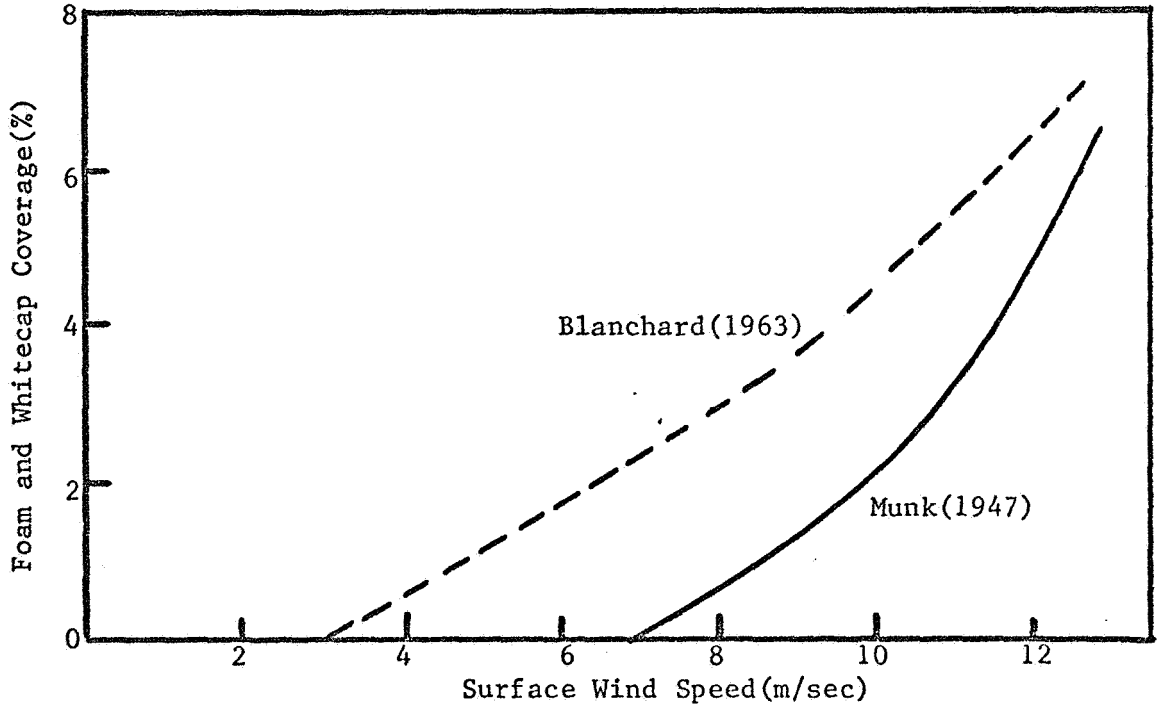

Fig. 2.9 Amount of foam and whitecap coverage as a function of surface wind speed.

Abe conclude that the foaming ability of sea water is the same everywhere offshore. However, this effect of salinity could explain the lower whitecap coverage for fresh water found by Monahan (1969), than was found by Blanchard (1963) for the ocean surface.

Monahan (1969) also determined the influence of atmospheric stability on the formation of whitecaps in his study. He found that whitecap coverage was greater when the atmosphere was unstable than when it was stable. Thus, even if it were possible to obtain identical oceanographic conditions, the amount of foam produced would be different if the thermal stability of the atmosphere was different between the cases.

The actual coverage of both whitecaps and foam have been determined by Blanchard (1963) and Munk (1947) as a function of the surface wind speed. The values obtained by Blanchard were given in terms of the percent coverage of the ocean surface by whitecaps; while those of Munk were in terms of the number of foam patches, and the area of the patches varied with the wind speed. Munk's values have been converted to percent coverage and the results of both authors are shown in Figure 2.9. It is obvious that both authors were not measuring the same thing. It should be noted that the values obtained by Munk for the first appearance of foam patches does agree closely with those values obtained by Monahan (1969) for fresh water whitecaps.

The stability of foam will be a function of the temperature of the water, the amount of organic matter present in the water and any films on the water surface. The results of Miyake and Abe (1948), shown in Figure 2.10, give the effect of temperature on the stability of foam. The

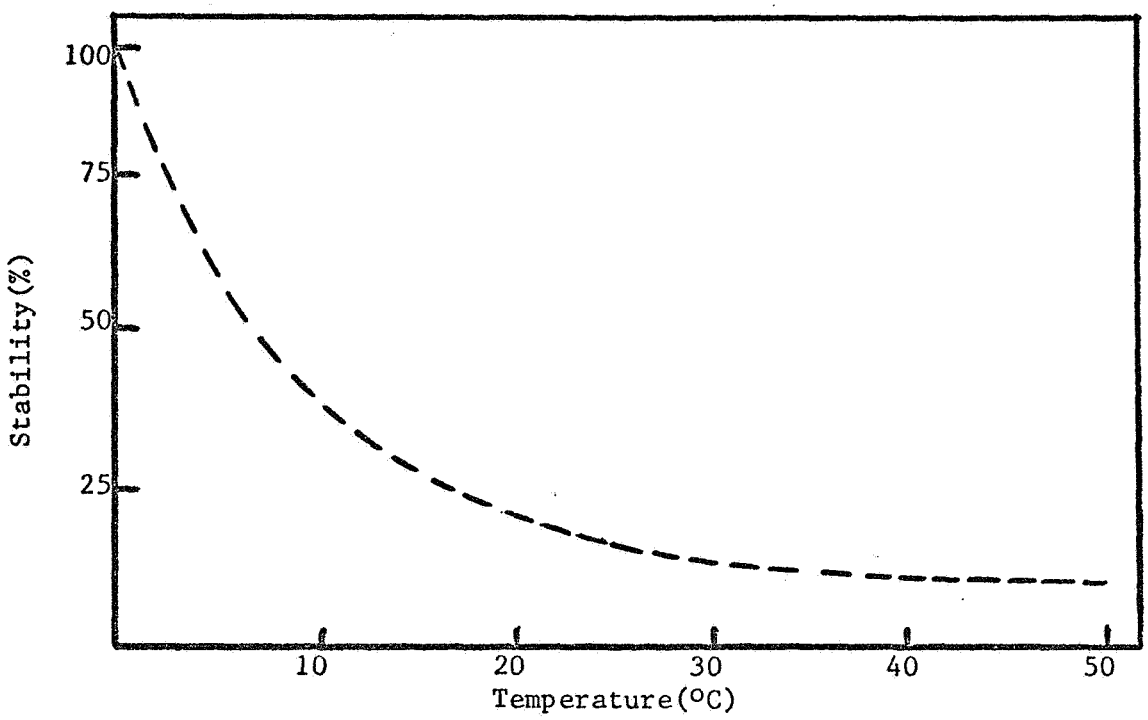

Fig. 2.10 Stability of sea foam with temperature(after Miyake and Abe,1948).

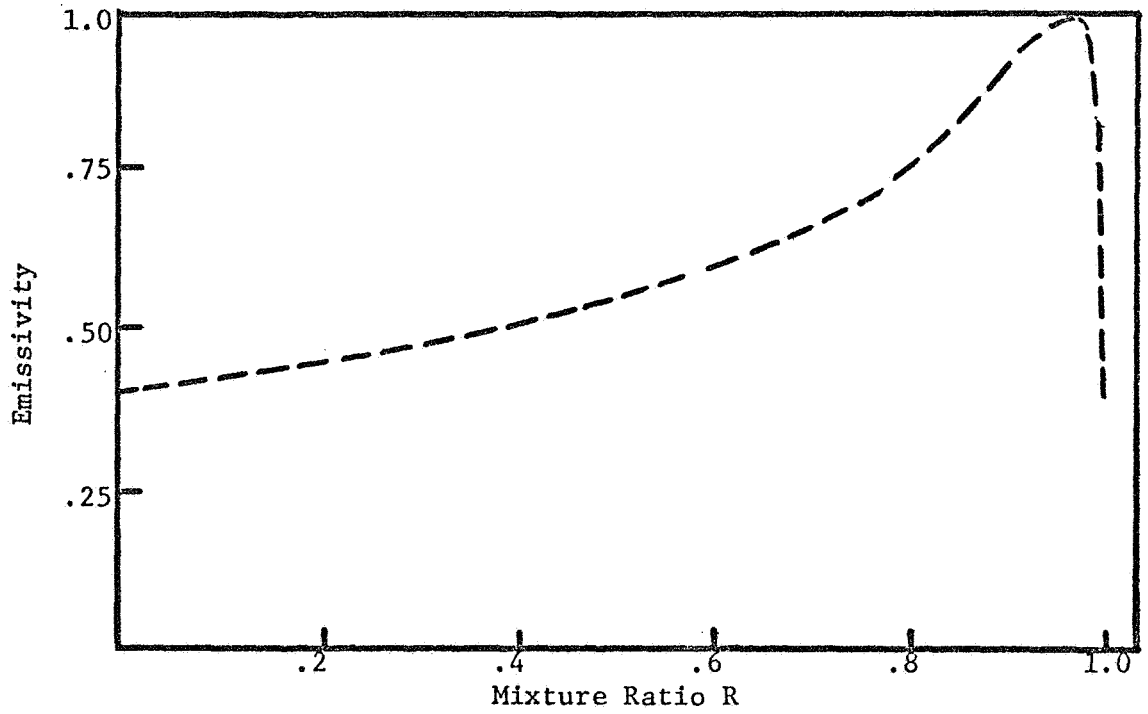

Fig. 2.11 Variation of emissivity of foam with mixture ratio R for a depth of one wavelength(after Droppleman,1970).

lifetime of a foamy layer at a temperature of 0°C was about 70 seconds and this time was reduced in half by a temperature increase to 10°C. Thus, the lifetime of foam will range from about 10 to 30 seconds, unless there is some means to stabilize the bubbles.

The effect of surface films and organic matter in the water on the stability of bubbles have been studied by Garrett (1967). He found that bubble stability can be increased by either the presence of surface films or by the adsorption of surface-active material on the bubbles as they pass through the bulk water. However, the second method is much more effective. Garrett also found that the presence of a monomolecular film will have the opposite effect, decreasing the bubble stability. This is due to the imbalance between the cohesive forces in the surface film and the changes in the surface tension, allowing potential rupture points to develop.

Of primary importance for radiometric observations is the dielectric constant of foam. Droppleman (1970) has made a theoretical calculation of the emissivity of foam using a simple model for the geometric and electrical properties. Treating foam as a porous material, the dielectric constant can be written as, (Odelevskii, 1962)

$$K = K_w\left[1 - \frac{3R}{\frac{3K_w+1}{K_w-1} + R}\right] \qquad 2.64$$

where K_w is the dielectric constant of water, the dielectric constant of air is assumed to equal 1.0, and R is the ratio of the volume of air to

the total volume of foam. Figure 2.11 shows the results obtained by Droppleman for the variation in emissivity at 19 GHz as a function of the mixture ratio R and for a depth of foam of one wavelength. The curve reaches a maximum value at about R = .98 and then drops rapidly to that of a plane water surface at R = 1.0 Kreiss (personal communication), has extended the work of Droppleman to other depths for a wavelength of 1.55 cm. His results for various depths are shown in Figure 2.12 and indicate that for thin layers of foam the maximum value of the emissivity is shifted toward lower R values and is lower in magnitude. There is also no smooth transition from one depth to another as far as the position of the maximum is concerned, although most maximum appears at R values from .95 to .98.

From the brief introduction above, it is evident that few generalizations can be made about the influence of foam on radiometric measurements. It is obvious that there will be little direct correlation between the surface wind speed and foam coverage, as too many other factors are involved. It is likely that foam depth will vary over the ocean surface. Near breaking waves the depth will probably be sufficient to provide high emissivity values, although shortlived. On the other hand, the persistent foam patches seen on the ocean surface will likely be smaller in depth and give emissivity values anywhere between that of a smooth water surface and a thick foam layer. Thus, the actual conditions will be a combination of the above, giving a wide range of emissivity values and, hence, brightness temperature variations.

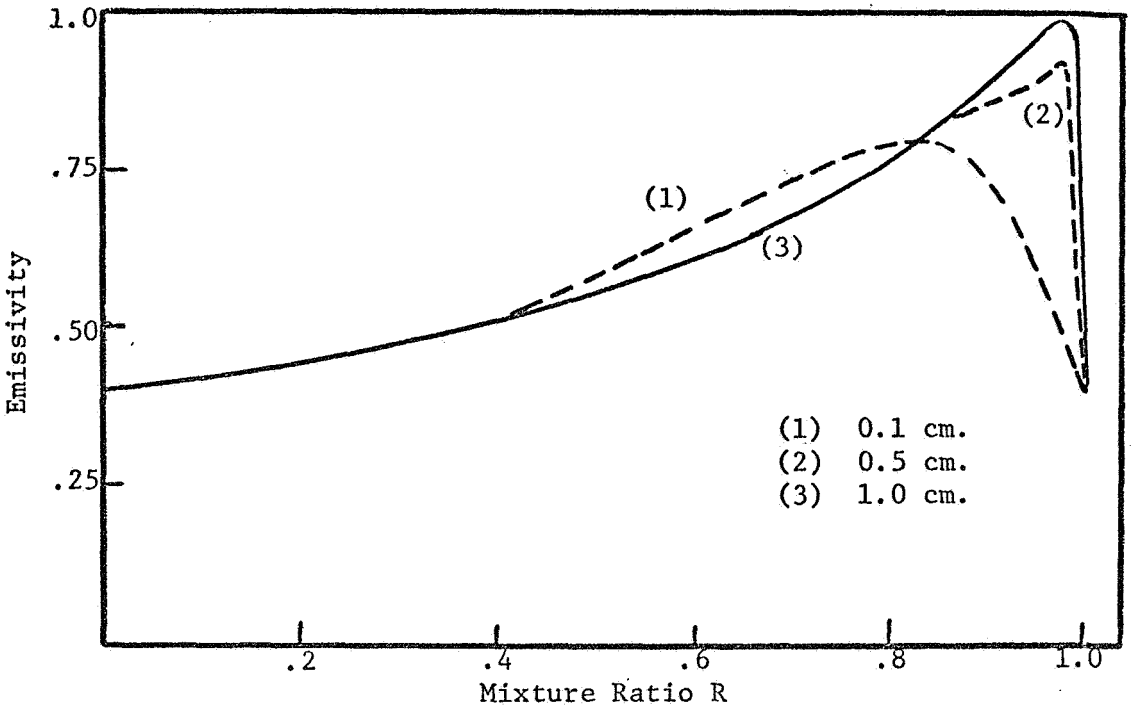

Fig. 2.12 Variation of emissivity of foam with mixture ratio R and depth of foam(after Kreiss, unpublished).

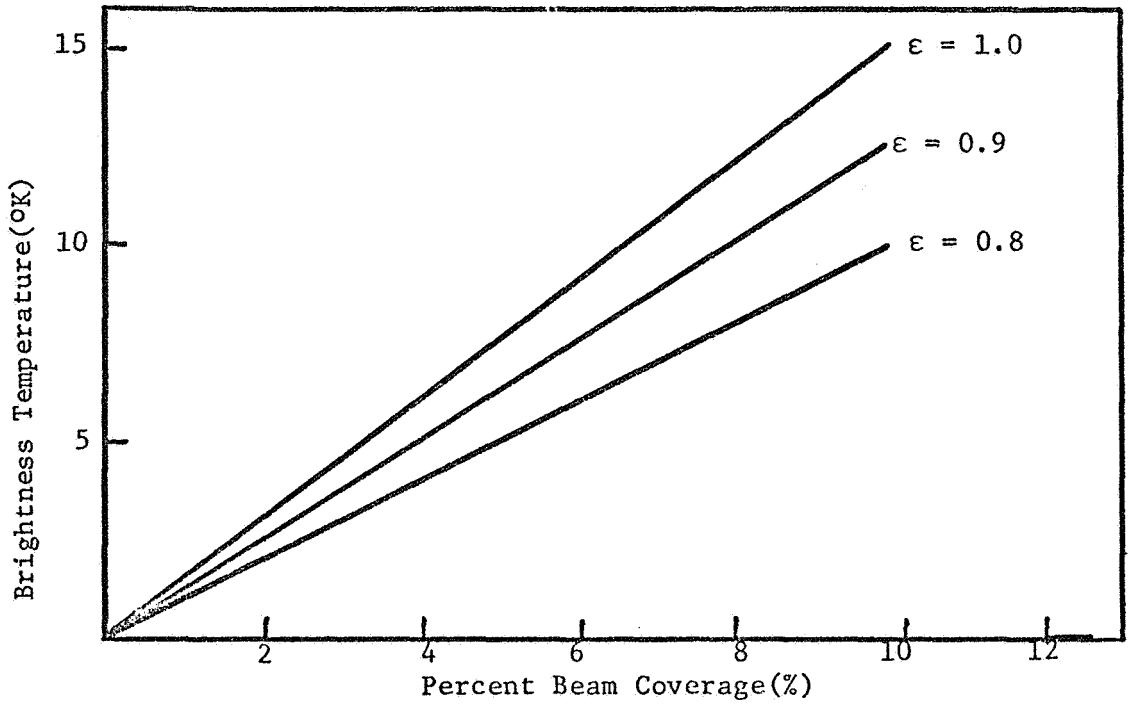

Fig. 2.13 Increase in brightness temperature due to foam on a smooth water surface.

To determine what brightness temperature increases might be expected with various foam coverages, calculations were made for the following conditions: 1) a specular surface covered with various percentages of foam; 2) various emissivities of foam, although constant with angle; 3) a standard atmosphere, and 4) an observer height of 35 km. One can then write that the emissivity of a specular surface covered with a certain percentage (A) of foam is

$$\varepsilon_w = A\varepsilon_f + (1-A)(1-|R_h|^2) \qquad 2.65$$

and the reflectivity becomes

$$r_w = A(1-\varepsilon_f) + (1-A)(|R_h|^2) \qquad 2.66$$

where εf is the emissivity of foam. The difference between the foam covered and the specular surface can then be written as

$$\Delta T = A\tau[T_g(\varepsilon_f - 1 + |R_h|^2) + (1-\varepsilon_f) \iint_{\Omega} T_{sky}(\theta)d\Omega - |R_h|^2 T_{sky}(\theta)] \qquad 2.67$$

The results obtained using equation 2.67 are shown in Figure 2.13. Using Munk's values in Figure 2.9 for the amount of coverage versus wind speed, the increase due to foam will only be about 3°K for wind speeds of 10 m/sec and assuming an emissivity of 1.0. Thus, for most wind speeds encountered over the oceans, the increase due to foam will be small and will be barely detectable over the normal variability of the signal.

2.12 Surface Films

Surface films have long been known to calm rough waters, their primary effect being to damp out the small scale capillary waves normally found on the sea surface. Cox and Munk (1954) determined the effect of oil slicks on the mean square slopes of the sea surface. For a clean surface their results were

$$g_x^2 = 0.003 + 1.92 \times 10^{-3} W \qquad 2.68$$

$$g_y^2 = 3.16 \times 10^{-3} W \qquad 2.69$$

and for a slick surface

$$g_x^2 = 0.003 + 0.84 \times 10^{-3} W \qquad 2.70$$

$$g_y^2 = 0.005 + 0.78 \times 10^{-3} W \qquad 2.71$$

where W is the wind speed at 41 feet above the water surface in m/sec. Thus, the mean square slopes are reduced by one-half to one-fourth by a slick covered surface and should prove to have a noticeable effect on brightness temperature measurements.

Auckland et al. (1970) made some measurements for slick covered surfaces at low wind speeds ($\leq$ 12 kts) and found decreases in brightness temperature of about 4°K. They estimate the effect for higher wind speeds will give decreases of up to 10°K.

One method of checking the expected decreases from theory is to use Stogryn's calculations for his rough surface model. His calculations for wind speeds of 4, 8, and 12 m/sec are equivalent to wind speeds of 9.8,

24. and 34.6 m/sec for a slick covered surface. Thus, the return from a slick covered surface and a wind speed of 9.8 m/sec is equivalent to that plotted for 4 m/sec. Interpolating between curves for what a clean surface at 10 m/sec would give, one can estimate that there will be an 8°K decrease at 50 degrees between the slick and clean surfaces. This difference will become smaller for viewing angles near nadir, but should increase for higher wind speeds. However, at high wind speeds the curves lose their angular dependence and the difference will be undetectable.

For thick films, the brightness temperatures will increase because the film is thick enough for its own dielectric constant to be important. Auckland et al. (1970) have found increases up to 100°K for a frequency of 35 GHz and for film thicknesses of 1.0 mm.

That these films are quite prevalent can be seen in both manned satellite and aerial photographs, especially along shipping lanes and around ports. According to Cox and Munk (1954), they are predominantly a low wind speed phenomena, as winds greater than 20 mph will cause them to break up.

CHAPTER 3

COMPUTATIONAL METHODS AND MODEL ATMOSPHERES

The preceding chapter has considered the theories for various factors involved in downward viewing observations of the ocean surface. In this chapter, some of the computational methods used in the calculations are described and four model atmospheres are introduced. These model atmospheres are used to provide information about the absorption due to oxygen and water vapor and are used to give an indication of the range of brightness temperature variations to be expected before actual observations are analyzed.

3.1 The Integrated Sky Temperature

The integrated sky temperature, which is needed for the reflected return from a diffuse surface, has been calculated in the following manner. This method saves computational time and yet provides sufficient accuracy. The reflected component was (equation 2.65)

$$r_s(\theta,\phi)T_{sky}(\theta) = \frac{\Gamma}{2}\int_0^{\pi/2} T_{sky}(\theta)\cos\theta d\theta \qquad 3.1$$

The sky temperature can be written as

$$T_{sky}(\theta) = T_m(1 - e^{-\alpha_o \sec\theta}) \qquad 3.2$$

where

T_m = mean temperature of the atmosphere

α_o = zenith absorption

This equation states that the sky temperature is just the emissivity of the atmosphere times the mean temperature of the atmosphere. Values of α_o and T_m were determined from the 14-layer atmospheric program to be described below. The values of sky temperature obtained using this method differs by less than one degree than those obtained using the entire 14-layer model and will be sufficient for our purposes.

3.2 Atmospheric Absorption and Emission

Atmospheric absorption and emission is determined by using the 14-layer model developed by Kreiss (1968), for his thesis. Two modifications have been made in his program, and the output has been changed to provide for additional information. The first modification involves the calculation of the average layer temperatures.

Kreiss calculated average layer temperatures using the hypsometric equation, which yields a pressure weighted average temperature. This equation is derived by combining the equation of state (eq. 2.22) and the hydrostatic equation (eq. 2.23) and writing

$$T(P)\frac{dP}{P} = -\frac{gdz}{R_d}$$

Upon integration over a finite layer, one obtains that

$$\bar{T}_i = \frac{H_{i+1} - H_i}{R_d/g \ \ln\left(\frac{P_i}{P_{i+1}}\right)}$$

where H_{i+1} and H_i are the geopotential height boundaries. To allow for the input of actual radiosonde data, which will be used in Chapter 5, average layer temperatures are calculated using the boundary temperatures for each layer and determining their average value. The effect of calculating the mean layer temperatures in this manner has been compared to those temperatures calculated using the hypsometric equation and agree to within 0.01 K.

The second modification was to use the most recent values for the constants in the water vapor absorption as determined by Gaut (1968) at MIT. These changes increased the absorption due to water vapor and increased the sky temperatures by approximately 1°K.

The output of the program provides the following information:

1. The transmissivity of each of the 14 layers, and hence, the total absorption of each layer for angles between 0 and 60 degrees in 10 degree increments.
2. The atmospheric contribution looking downward from the top of each layer and for the above angles.
3. The total sky temperature for each of the above angles.
4. The total transmissivity of the atmosphere for each of the above angles.
5. The total brightness temperature looking downward for:
   a. observer heights of 1, 3 and 35 km.
   b. angles from 0 to 60 degrees in 10 degree intervals
   c. both specular and diffuse surfaces

A copy of the program, a list of the output symbols, and a sample output is included at the end of this chapter.

3.3 Model Atmospheres

To check out the program and provide an indication of the range of brightness temperatures to be expected, four model atmospheres were used with the program before actual data analysis was started. The four models involve combinations of two temperature and two relative humidity profiles. These models are those used by Kreiss in his thesis and have been chosen to represent conditions which might be found over the oceans.

The first temperature profile is the U. S. Standard Atmosphere (1962) and the second is one that is labeled hot and differs from the standard atmosphere by having warmer tropospheric temperatures. Table 3.1 gives the pressure versus geopotential height and pressure versus kinetic temperature for the standard atmospheric model, along with the mean layer temperatures. Table 3.2 provides the same data for the hot atmospheric model.

Water vapor is introduced into the models by specifying the mean relative humidity for each layer. The same relative humidity profile is used for each model, but because of the temperature differences between models, the absolute humidity values are different. Two humidity profiles are used, the first labeled standard and the second called wet, which is 1.25 times the standard profile. The relative and absolute humidity values for each model are given in Table 3.3.

Table 3.1 Standard model atmosphere

Press(mb)	Geopotential Ht(km)	Kinetic Temp(K)	Mean Temp(K)
1013.25	0.00000	288.15	287.24
980.00	0.28053	286.33	285.20
950.00	0.62842	284.07	282.90
900.00	0.98850	281.73	280.21
850.00	1.45730	278.68	277.08
800.00	1.94899	275.48	273.80
750.00	2.46622	272.12	270.35
700.00	3.01218	268.57	264.69
600.00	4.20643	260.81	256.37
500.00	5.57444	251.92	246.69
400.00	7.18544	241.45	235.02
300.00	9.16396	228.58	222.63
200.00	11.77490	216.65	216.65
100.00	15.79731	216.65	226.16
5.00	35.77651	235.68	

Table 3.2 Hot model atmosphere

Press(mb)	Geopotential Ht(km)	Kinetic Temp(K)	Mean Temp(K)
1013.25	0.00000	304.25	302.77
980.00	0.29570	301.29	299.46
950.00	0.66099	297.64	295.75
900.00	1.03744	293.88	291.44
850.00	1.52504	289.00	286.45
800.00	2.03336	283.92	281.25
750.00	2.56468	278.60	275.81
700.00	3.12168	273.03	266.96
600.00	4.32627	260.99	254.15
500.00	5.68259	247.42	239.52
400.00	7.24704	231.78	222.65
300.00	9.12190	216.65	216.65
200.00	11.69321	216.65	216.65
100.00	16.08888	216.65	223.37
5.00	35.67627	238.94	

Table 3.3 Water vapor profiles

STANDARD ATMOSPHERE

Stnd Profile		Wet Profile	
Rel Hum(%)	Abs Hum(g/m^3)	Rel Hum(%)	Abs Hum(g/m^3)
58	7.03	73	8.85
60	6.41	75	8.01
61	5.64	76	7.02
66	5.13	83	6.45
68	4.30	85	5.38
75	3.80	94	4.76
70	2.79	88	3.50
60	1.59	75	1.98
59	0.82	74	1.03
60	0.37	75	0.46
60	0.13	75	0.16
35	0.01	44	0.02
15	0.00	19	0.00
05	0.00	06	0.00

HOT ATMOSPHERE

Stnd Profile		Wet Profile	
Rel Hum(%)	Abs Hum(g/m^3)	Rel Hum(%)	Abs Hum(g/m^3)
58	17.27	73	21.73
60	14.89	75	18.61
61	12.27	76	15.29
66	10.32	83	12.97
68	7.86	85	9.82
75	6.24	94	7.82
70	4.07	88	5.11
60	1.88	75	2.35
59	0.69	74	0.87
60	0.20	75	0.25
60	0.03	75	0.03
35	0.01	44	0.01
15	0.00	19	0.00
05	0.00	06	0.00

3.4 Computational Cases

Computations have been made using combinations of the two temperature and relative humidity profiles to provide information about the following:

1. Altitude dependence and angular variation of brightness temperature.
2. The effect of surface roughness.
3. The effect of temperature and water vapor profiles, including the temperature dependence of the absorption due to oxygen and water vapor.

The specific cases for which computations have been made are listed below:

1. Standard temperature and standard RH provile.
2. Standard temperature and wet RH profile.
3. Hot temperature and standard RH profile.
4. Hot temperature and wet RH profile.
5. Standard and hot temperature profiles and zero RH.
6. Hot temperature and standard absolute RH values.

Computations have been made of these cases, and the results, along with a discussion and an analysis, are presented in the following chapter.

LIST OF OUTPUT SYMBOLS

The following is a list of the output symbols used in the calculation of the theoretical brightness temperatures.

A(I,J) = transmissivity of each atmospheric layer

TA(I,J) = brightness temperature contribution of each atmospheric layer

TS(I) = total sky temperature

TT(I) = total atmospheric transmissivity

TB(I,1) = total brightness temperature for specular surface and height of 1 kilometer

TBD(I,1) = total brightness temperature for diffuse surface and height of 1 kilometer

TB(I,2) = total brightness temperature for specular surface and height of 3 kilometers

TBD(I,2) = total brightness temperature for diffuse surface and height of 3 kilometers

TB(I,3) = total brightness temperature for specular surface and height of 35 kilometers

TBD(I,3) = total brightness temperature for diffuse surface and height of 35 kilometers.

```
      DIMENSION P(16),RH(16),T(16),BI(15),AT(7,14),TM(15),RHM(15),A(15),
     1TE(7,14),TA(7,14),TS(7),TT(7),TR(7,3),TB(7,3),TBD(7,3),R(7),AM(7,3
     1)
      COMMON IZ
101   FORMAT(8F8.2)
102   FORMAT(7F7.2)
104   FORMAT(1H1,4X,6HA(1,J),4X,6HA(2,J),4X,6HA(3,J),4X,6HA(4,J),4X,6HA(
     15,J),4X,6HA(6,J),4X,6HA(7,J)//)
105   FORMAT(7F10.4/)
106   FORMAT(1H1,3X,7HTA(1,J),3X,7HTA(2,J),3X,7HTA(3,J),3X,7HTA(4,J),3X,
     17HTA(5,J),3X,7HTA(6,J),3X,7HTA(7,J)//)
107   FORMAT(7F10.2/)
108   FORMAT(1H0,5X,5HTS(1),5X,5HTS(2),5X,5HTS(3),5X,5HTS(4),5X,5HTS(5),
     15X,5HTS(6),5X,5HTS(7)//)
109   FORMAT(1H0,5X,5HTT(1),5X,5HTT(2),5X,5HTT(3),5X,5HTT(4),5X,5HTT(5),
     15X,5HTT(6),5X,5HTT(7)//)
110   FORMAT(7F10.5/)
111   FORMAT(1H1,3X,7HTR(I,1),3X,7HTR(I,2),3X,7HTR(I,3)//)
112   FORMAT(3F10.5/)
113   FORMAT(1H0,3X,7HTB(I,1),2X,8HTBD(I,1),3X,7HTB(I,2),2X,8HTBD(I,2),3
     1X,7HTB(I,3),2X,8HTBD(I,3)//)
114   FORMAT(6F10.2/)
115   FORMAT(7F10.4)
      IZ = 1
      RD = 0.5656
      TG = 288.0
      TSK = 23.00
      READ(5,101)(P(I),I=1,15)
      READ(5,102)(RHM(I),I=1,14)
      READ(5,101)(T(I),I=1,15)
      READ(5,115)(R(I),I=1,7)
      F = 19.35
      DO 1 I=1,15
      IF(P(I) - 400.)2,3,3
3     BI(I) = 0.25
      GO TO 1
2     BI(I) = 1. - .75*SQRT(1. - ((400.-P(I))/400.)**2.)
1     CONTINUE
      DO 9 J=1,14
```

```
      TM(J) = (T(J) + T(J+1))/2.
9     CONTINUE
      DO 20 J=1,14
      CALL TRANFU(P(J),BI(J),P(J+1),BI(J+1),RHM(J),TM(J),F,A(J))
      X = 0.0
      DO 25 I=1,7
      AT(I,J) = EXP(-A(J)/COS(X))
      TE(I,J) = (1. - AT(I,J))*TM(J)
      X = X + 0.17453
25    CONTINUE
20    CONTINUE
      WRITE(6,104)
      DO 30 J=1,14
      WRITE(6,105)AT(1,J),AT(2,J),AT(3,J),AT(4,J),AT(5,J),AT(6,J),AT(7,J
     1)
30    CONTINUE
      DO 55 I=1,7
      TA(I,1) = TE(I,1)
      TA(I,2) = TA(I,1)*AT(I,2) + TE(I,2)
      TA(I,3) = TA(I,2)*AT(I,3) + TE(I,3)
      AM(I,1) = TA(I,3)
      TA(I,4) = TA(I,3)*AT(I,4) + TE(I,4)
      TA(I,5) = TA(I,4)*AT(I,5) + TE(I,5)
      TA(I,6) = TA(I,5)*AT(I,6) + TE(I,6)
      TA(I,7) = TA(I,6)*AT(I,7) + TE(I,7)
      AM(I,2) = TA(I,7)
      TA(I,8) = TA(I,7)*AT(I,8) + TE(I,8)
      TA(I,9) = TA(I,8)*AT(I,9) + TE(I,9)
      TA(I,10) = TA(I,9)*AT(I,10) + TE(I,10)
      TA(I,11) = TA(I,10)*AT(I,11) + TE(I,11)
      TA(I,12) = TA(I,11)*AT(I,12) + TE(I,12)
      TA(I,13) = TA(I,12)*AT(I,13) + TE(I,13)
      TA(I,14) = TA(I,13)*AT(I,14) + TE(I,14)
      AM(I,3) = TA(I,14)
      T1 = AT(I,1)*AT(I,2)*AT(I,3)
      TR(I,1) = T1
      T2 = T1*AT(I,4)
      T3 = T2*AT(I,5)
```

```
      T5 = T4*AT(I,7)
      TR(I,2) = T5
      T6 = T5*AT(I,8)
      T7 = T6*AT(I,9)
      T8 = T7*AT(I,10)
      T9 = T8*AT(I,11)
      T10 = T9*AT(I,12)
      T11 = T10*AT(I,13)
      TT(I) = T11*AT(I,14)
      TR(I,3) = TT(I)
      TS(I) = TE(I,1) + TE(I,2)*AT(I,1) + TE(I,3)*AT(I,1)*AT(I,2) + TE(I
     1,4)*T1 + TE(I,5)*T2 + TE(I,6)*T3 + TE(I,7)*T4 + TE(I,8)*T5 + TE(I,
     19)*T6 + TE(I,10)*T7 + TE(I,11)*T8 + TE(I,12)*T9 + TE(I,13)*T10 + T
     1E(I,14)*T11
55    CONTINUE
      WRITE(6,106)
      DO 75 J=1,14
      WRITE(6,107)TA(1,J),TA(2,J),TA(3,J),TA(4,J),TA(5,J),TA(6,J),TA(7,J
     1)
75    CONTINUE
      WRITE(6,108)
      WRITE(6,107)TS(1),TS(2),TS(3),TS(4),TS(5),TS(6),TS(7)
      WRITE(6,109)
      WRITE(6,110)TT(1),TT(2),TT(3),TT(4),TT(5),TT(6),TT(7)
      WRITE(6,111)
      DO 31 I=1,7
      WRITE(6,112) TR(I,1),TR(I,2),TR(I,3)
31    CONTINUE
      DO 32 J=1,3
      DO 33 I=1,7
      TR(I,J) = ((1. - R(I))*TG + R(I)*TS(I))*TR(I,J) + AM(I,J)
      TBD(I,J) = ((1.- RD)*TG + 2.*RD*TSK)*TR(I,J) + AM(I,J)
33    CONTINUE
32    CONTINUE
      WRITE(6,113)
      DO 36 I=1,7
      WRITE(6,114)TR(I,1),TBD(I,1),TB(I,2),TBD(I,2),TB(I,3),TBD(I,?)
36    CONTINUE
      END
```

```
      SUBROUTINE TRANFU(P1,B1,P2,B2,RH,T,D,A)
      DIMENSION B(45),C(45)
      COMMON IZ
      IF(IZ-2)44,44,45
44    B(1)=56.2648
      C(1)=118.7505
      B(2)=58.4466
      C(2)=62.4863
      B(3)=59.5910
      C(3)=60.3061
      B(4)=60.4348
      C(4)=59.1642
      B(5)=61.1506
      C(5)=58.3239
      B(6)=61.8002
      C(6)=57.6125
      B(7)=62.4112
      C(7)=56.9682
      B(8)=62.9980
      C(8)=56.3634
      B(9)=63.5685
      C(9)=55.7839
      B(10)=64.1272
      C(10)=55.2214
      B(11)=64.6779
      C(11)=54.6728
      B(12)=65.2240
      C(12)=54.1294
      B(13)=65.7626
      C(13)=53.5960
      B(14)=66.2978
      C(14)=53.0695
      B(15)=66.8313
      C(15)=52.5458
      B(16)=67.3627
      C(16)=52.0259
      B(17)=67.8923
      C(17)=51.5091
      B(18)=68.4205
```

```
      C(18)=50.9949
      B(19)=68.9478
      C(19)=50.4830
      B(20)=69.4741
      C(20)=49.9730
      B(21)=70.0000
      C(21)=49.4648
      B(22)=70.5249
      C(22)=48.9582
      B(23)=71.0497
      C(23)=48.4530
      DO 46 I=1,45,2
      J = (I+1)/2
      B(46-I) = B(24-J)
      C(46-I) = C(24-J)
46    CONTINUE
      IZ = IZ + 2
45    CONTINUE
      T2 = 0.0
      G = 980.665
      Q = 2.8704E6
      B6 = 0.0
      PP = (P1+P2)/2.
      BB = (B1+B2)/2.
      IF(RH-0.0)7,7,29
29    X1 = 1.32405E3/T
      IF(T-233.)39,49,49
49    IF(T-273.16)59,79,79
79    X2 = 2.501E10-9.7E6*(T-273.16)
      GO TO 99
59    X2 = 2.501E10-1.3E7*(T-273.16)
      GO TO 99
39    X2 = 2.835E10-7.0E5*(T-273.16)
99    X3 = (X2/4.615E6)*(T-273.16)/(T*273.16)
      RHO = RH*X1*EXP(X3)
      Q = Q*(1.+((2.8704E-3*RHO*T)/(.622*PP)))/(1.+(2.8704E-3*RHO*T)/PP)
      A5 = 2.580E-3*PP*(318./T)**0.625*(1.+.046*(T/PP)*RHO)
      A6 = 1./((22.235-D)**2+A5**2)
      A7 = 1./((D+22.235)**2+A5**2)
```

```
      B2 = Q*T/G
      B4 = 2.55E-8*RHO*D**2*A5*T**(-1.5)
      B7 = 3.615E-3*EXP(-642./T)*D**2.*RHO*T**(-2.5)*A5
      B6 = B3*(B7*(A6+A7)+B4*A5)*ALOG(P1/P2)
    7 C1 = 0.61576E-5*760./1013.25
      C2 = 0.195E-2*760./1013.25
      C3 = C2*.21*300.**0.85
      C4 = C2*.78*300.**0.85
      R1 = Q*C1/G
      A1 = (C3+C4*B1)/T**0.85
      A4 = (C3+C4*B2)/T**0.85
      A2 = A1*P1
      A3 = A4*P2
      DO 96 L=1,45,2
      K = L
      F1 = (B(L)+D)**2+A2**2
      F2 = (B(L)-D)**2+A2**2
      G1 = (C(L)+D)**2+A2**2
      G2 = (C(L)-D)**2+A2**2
      F4 = (B(L)+D)**2+A3**2
      F5 = (B(L)-D)**2+A3**2
      G3 = (C(L)+D)**2+A3**2
      G4 = (C(L)-D)**2+A3**2
      F6 = D**2+A2**2
      F7 = D**2+A3**2
      AN = K*(2*K+3)/(K+1)
      BN = (K+1)*(2*K-1)/K
      CN = 2*(K**2+K+1)*(2*K+1)/(K*(K+1))
      AK = AN*ALOG(F1*F2/(F4*F5))
      BK = BN*ALOG(G1*G2/(G3*G4))
      CK = CN*ALOG(F6/F7)
      E1 = R1*EXP(-2.06844*K*(K+1)/T)*T**0.85/(2.0*(C3+C4*BB))
      S1 = (AK+BK+CK)*E1*D**2
      T2 = T2 + S1
      A = T2/T**2
      IF(45-K)89,89,96
   89 T2 = 0.0
      A = A + B6
   96 CONTINUE
      RETURN
```

A(1,J)	A(2,J)	A(3,J)	A(4,J)	A(5,J)	A(6,J)	A(7,J)
.9903	.9902	.9897	.9889	.9874	.9850	.9808
.9921	.9920	.9916	.9909	.9897	.9877	.9842
.9864	.9862	.9877	.9806	.9849	.9821	.9770
.9893	.9891	.9886	.9876	.9860	.9834	.9787
.9910	.9908	.9904	.9896	.9882	.9861	.9820
.9919	.9918	.9914	.9907	.9895	.9875	.9839
.9939	.9938	.9935	.9930	.9921	.9905	.9879
.9926	.9925	.9921	.9915	.9904	.9886	.9853
.9956	.9956	.9954	.9950	.9943	.9932	.9913
.9975	.9975	.9973	.9971	.9967	.9961	.9950
.9987	.9987	.9986	.9985	.9983	.9980	.9975
.9994	.9994	.9994	.9993	.9992	.9991	.9988
.9996	.9996	.9995	.9995	.9995	.9994	.9992
.9998	.9998	.9998	.9998	.9998	.9997	.9996

TA(1,J)	TA(2,J)	TA(3,J)	TA(4,J)	TA(5,J)	TA(6,J)	TA(7,J)
2.77	2.82	2.95	3.20	3.62	4.33	5.52
5.01	5.08	5.33	5.77	6.52	7.75	9.93
8.23	8.35	8.75	9.48	10.69	12.69	16.21
11.14	11.31	11.84	12.82	14.45	17.14	21.84
13.54	13.74	14.38	15.57	17.54	20.77	26.42
15.64	15.87	16.61	17.98	20.24	23.95	30.43
17.19	17.45	18.25	19.75	22.22	26.23	33.31
19.02	19.30	20.19	21.84	24.56	29.01	36.71
20.05	20.35	21.29	23.02	25.88	30.55	38.63
20.62	20.92	21.89	23.66	26.60	31.39	39.67
20.89	21.20	22.17	23.97	26.94	31.79	40.16
21.01	21.32	22.30	24.11	27.09	31.97	40.38
21.09	21.40	22.38	24.20	27.19	32.08	40.52
21.13	21.44	22.42	24.24	27.24	32.14	40.59

TS(1)	TS(2)	TS(3)	TS(4)	TS(5)	TS(6)	TS(7)
21.17	21.48	22.47	24.29	27.31	32.23	40.74

TT(1)	TT(2)	TT(3)	TT(4)	TT(5)	TT(6)	TT(7)
.92305	.92192	.91832	.91169	.90076	.88289	.85203

TR(I,1)	TR(I,2)	TR(I,3)
.97113	.93863	.92305
.97069	.93772	.92192
.96931	.93482	.91832
.96674	.92948	.91169
.96249	.92065	.90076
.95545	.90617	.88289
.94310	.88103	.85203

TB(I,1)	TBD(I,1)	TB(I,2)	TBD(I,2)	TB(I,3)	TBD(I,3)
134.01	150.14	138.77	154.36	140.69	156.02
133.05	150.20	137.93	154.48	139.87	156.16
130.18	150.40	135.37	154.87	137.47	156.62
125.58	150.75	131.38	155.58	133.74	157.47
119.00	151.34	126.40	156.76	129.16	158.87
113.09	152.32	121.43	158.70	124.91	161.16
108.17	154.03	119.22	162.06	123.67	165.10

CHAPTER 4

COMPUTATIONAL RESULTS

This chapter gives the results for the computational cases listed in the previous chapter. The effect of the atmosphere will be considered first, and then the total brightness temperatures observed for various surface features and atmospheric profiles will be discussed.

4.1 The Atmosphere

Figures 4.1 and 4.2 show the absorption with height for each of the model atmospheres, i.e., both the standard and hot temperature profiles with the standard and wet RH profiles. For comparison, the absorption as a function of height used by Stogryn (1967) has been plotted in Figure 4.1. His curve differs from the models used in this study by the amount of water vapor present, since the temperature profiles used were almost identical.

The above figures show the effect of water vapor, with increasing water vapor giving higher absorption. The effect of temperature on the absorption due to water vapor was determined by calculating the mean absolute humidity values for the standard relative humidity profile and then using these values with the hot temperature profile. This meant that the total amount of water vapor was the same in each case and only the temperature profile differed. This calculation was made and the resulting difference between the cases was negligible, amounting to less than 0.3°K in

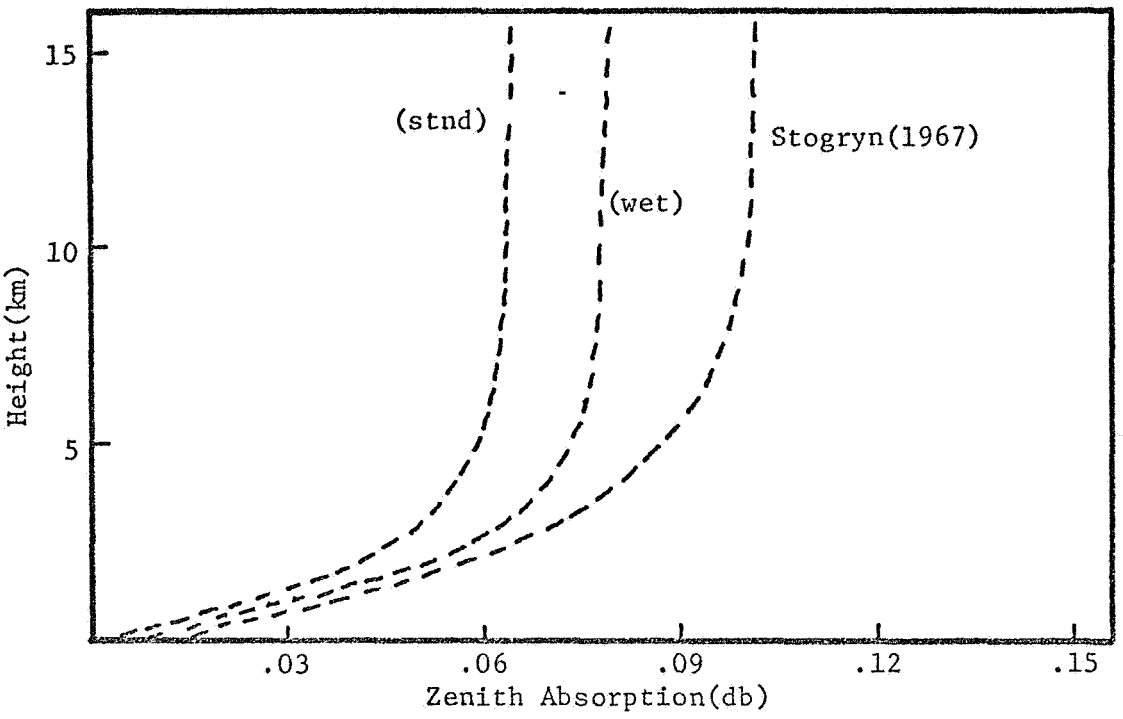

Fig. 4.1 Absorption versus height for standard temperature profile and standard and wet relative humidity profiles.

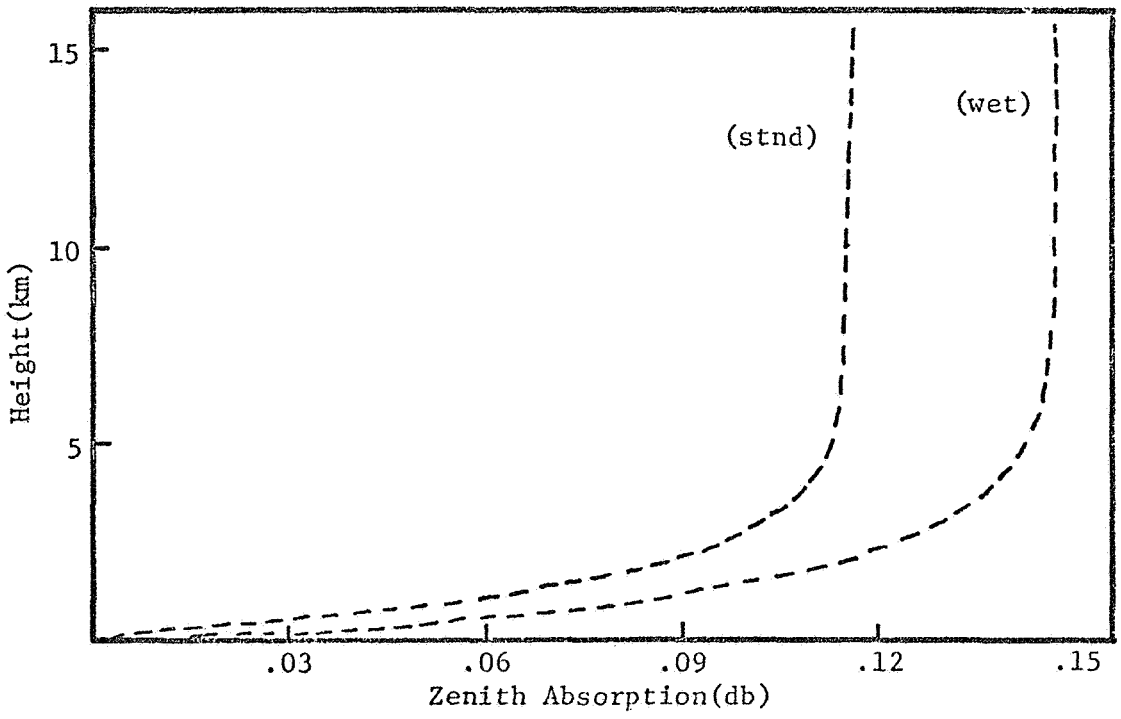

Fig. 4.2 Absorption versus height for hot temperature profile and standard and wet relative humidity profiles.

total observed sky temperature. Thus, one can conclude that, for temperatures normally encountered in the atmosphere, and at a frequency of 19.35 GHz, the absorption due to water vapor is dependent only on the amount of water vapor present, and not on the temperature profile.

The effect of temperature on the absorption due to oxygen was also investigated. This was done by running the program with no water vapor at all for the two temperature profiles. The difference between these two cases amounted to 0.03°K in sky temperature. Thus, the influence of temperature on the absorption due to oxygen is also negligible for normal atmospheric temperatures and at a frequency of 19.35 GHz.

4.2 Brightness Temperature Variations

The total downward viewing brightness temperature for all four model atmospheres is shown in Figures 4.3-4.6. Values are shown for two observer heights (1 and 35 km) and for both specular and diffuse surface roughness. For all cases the surface temperature has been assumed to be 288°K. The following can be noticed from the curves:

1. For a specific surface, high altitude observations give temperature increases of 6 to 8°K over observations made at lower altitudes, with higher values being obtained with increasing water vapor content of the atmosphere.
2. Surface roughness is an important factor in both the expected magnitude and angular variation of the brightness temperature. Diffuse surfaces give increases of 14 to 16°K over those from a specular surface, depending on the water vapor content of the atmosphere.

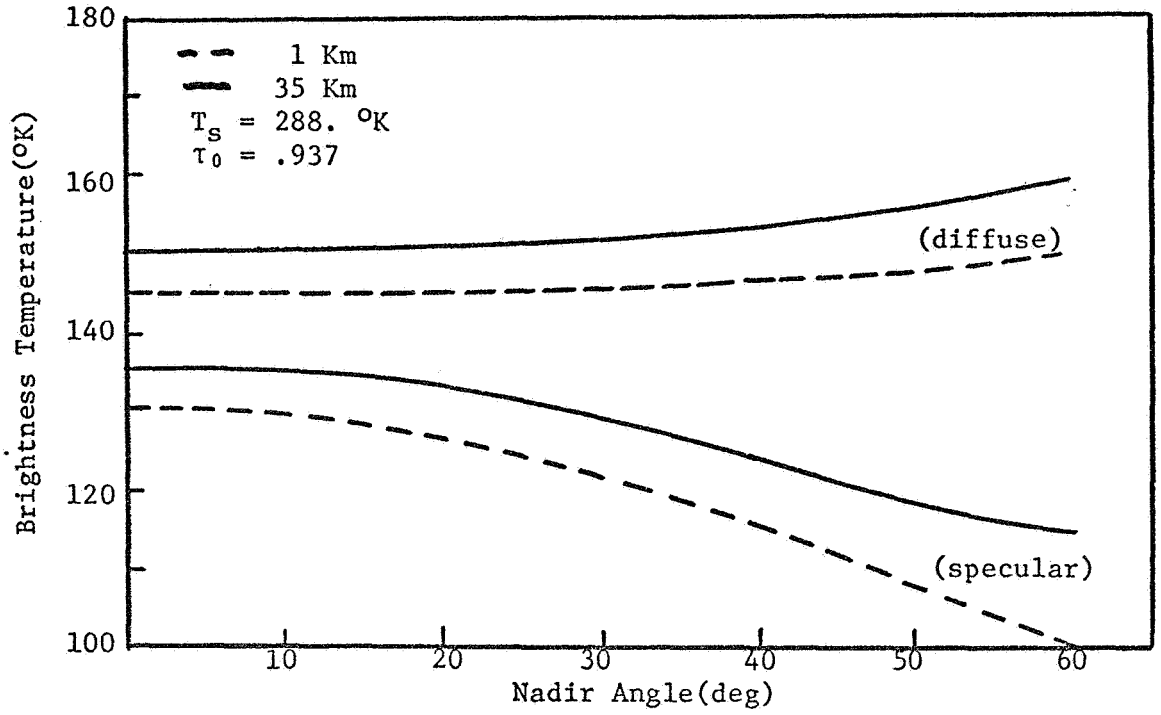

Fig. 4.3 Angular variation of brightness temperature for standard temperature and relative humidity profiles.

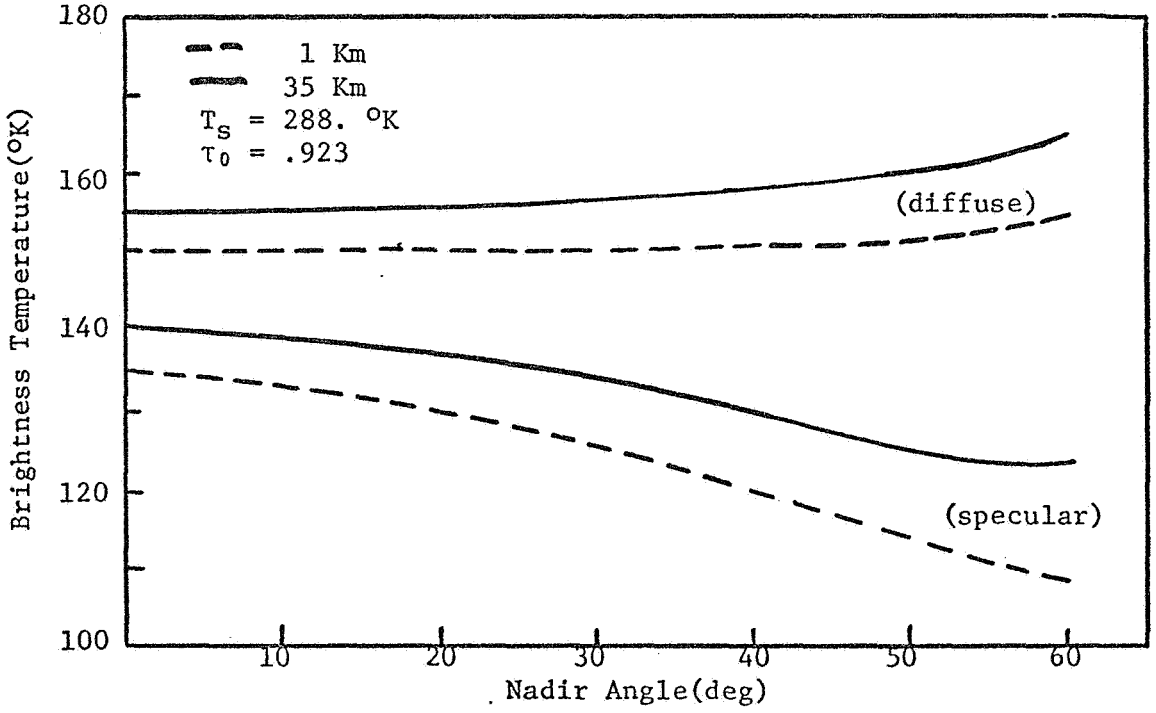

Fig. 4.4 Angular variation of brightness temperature for standard temperature and wet relative humidity profiles.

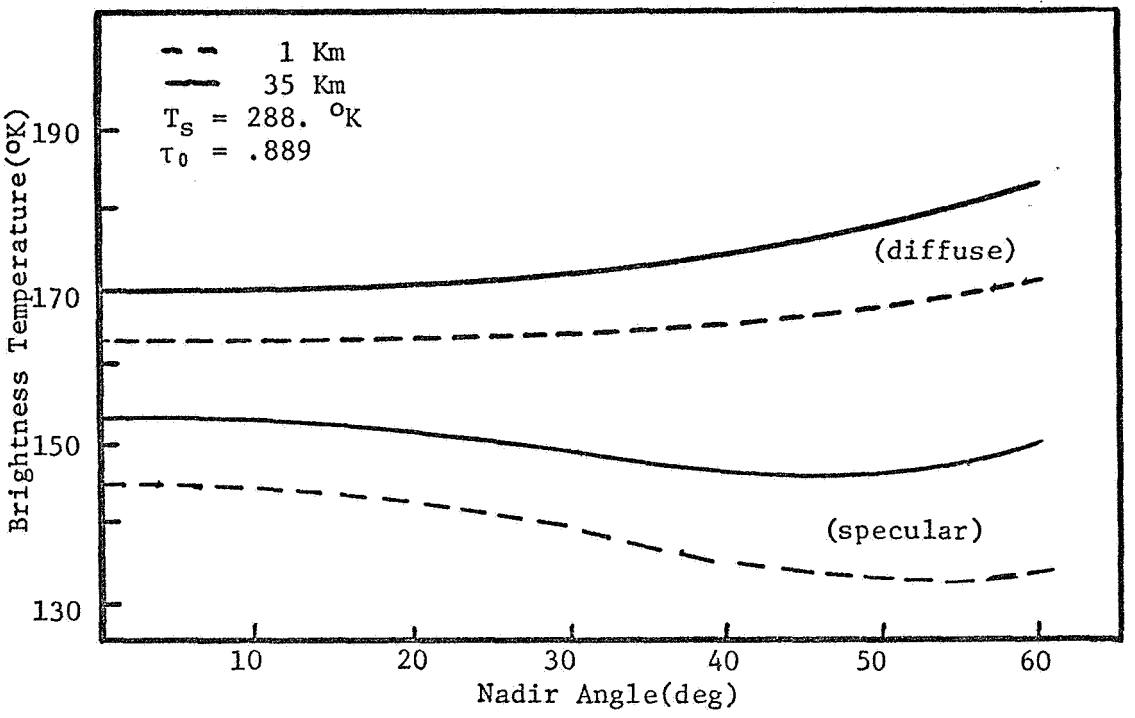

Fig. 4.5 Angular variation of brightness temperature for hot temperature and standard relative humidity profiles.

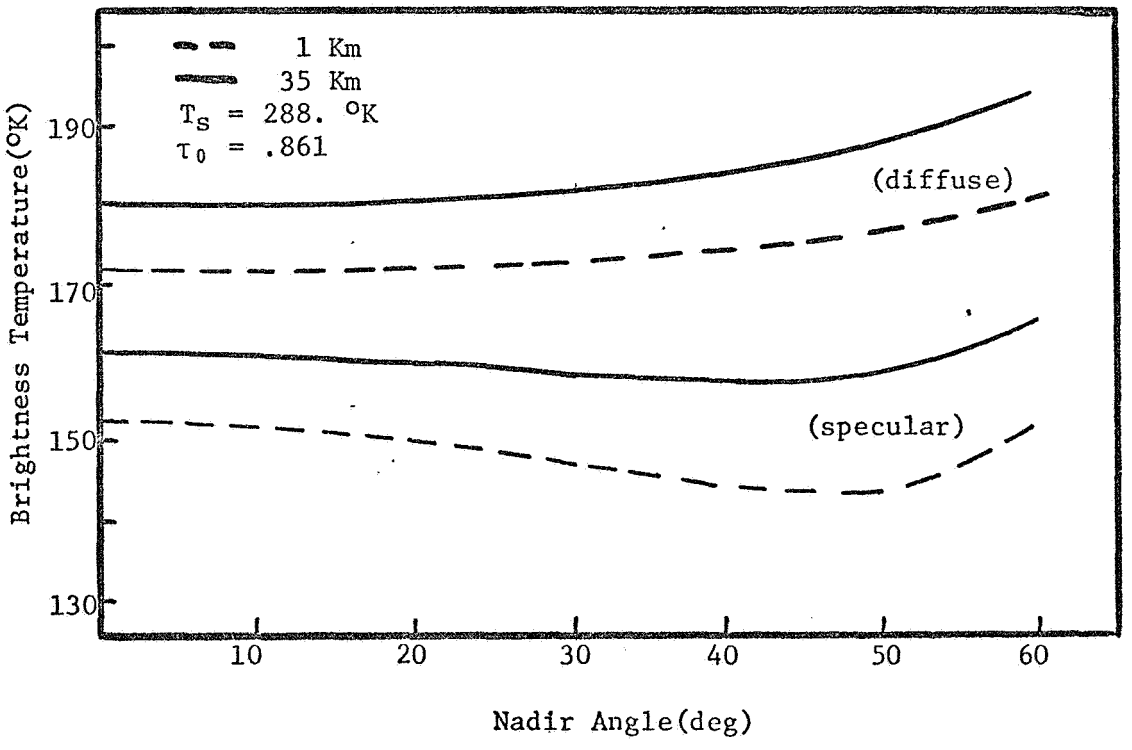

Fig. 4.6 Angular variation of brightness temperature for hot temperature and wet relative humidity profiles.

3. For high transmissivities, the specular surface decreases with angle, reaching a minimum value beyond 60 degrees, whereas the diffuse surface curves are generally flat with increasing viewing angle. As the transmissivity becomes smaller (i.e., increasing absorption), the specular curves become flatter and the minimum is shifted toward smaller viewing angles. The effect on the diffuse curves is to give increasing temperatures at large viewing angles.
4. Surface temperature variations have been considered in Chapter 2, and provide only 2°K differences in surface emission. For this reason and the fact that the normal variations in signal exceed 2°K, these curves have not been plotted.
5. The difference in water vapor content between the models can contribute up to 25°K difference in brightness temperature for the same surface roughness and observing height.

Thus, it can be seen that altitude, surface roughness and atmospheric water vapor are all extremely important in brightness temperature measurements. None of these factors can be neglected in analyzing data or determining information about the atmosphere or the ocean surface. The effect of water vapor and the altitude variations can be found from measurements of the water vapor content of the atmosphere; and once these are known, information about the roughness of the surface can be obtained.

The following chapter considers observations taken with a 19.35 GHz radiometer and the analysis of the data considering the above factors.

CHAPTER 5

OBSERVATIONS

In this chapter, downward viewing radiometric observations obtained by NASA personnel (Catoe et al., 1967) at 19.35 GHz are described and analyzed. Comparison is then made to the theoretical calculations of the expected brightness temperatures using various surface roughness models and atmospheric temperature and relative humidity profiles obtained from actual synoptic data. The purpose is to determine how well current theories can explain the observed data under various surface and atmospheric conditions.

5.1 The observing system

The observations to be described below have been taken by a Convair 990 jet aircraft using an antenna of 2.7° beamwidth which is scanned electrically ±50° normal to the aircraft's flight path. The scan is from left to right (a total of 100 degrees) and is taken every two seconds, providing a contigious map of the earth's surface, depending on the aircraft's altitude. Each scan is divided into 39 data points, with data point 20 being vertical viewing. Polarization of the antenna is horizontal, or such that the electric vector is always parallel to the earth's surface. Sensitivity of the radiometer is purported to be 2°K, with a smoothing time of 0.05 secs. Along with the radiometer output,

black and white photographs, with a 74 degree field of view, were taken every 15 seconds to provide for interpretation of the data.

5.2 Atmospheric profiles

Observations have been taken from two flights made during the spring of 1967; Flights #6 and #13, and one flight over the Salton Sea on 7 June 1968. Flight #6 was taken on 29 May and covered portions of the Pacific Ocean near the northern coast of California. Flight #13 was made on 6 June 1967, and covered the northern portion of the Gulf of Mexico. Although the maximum surface wind speed encountered on these flights was about 20 kts, both the atmospheric profiles and the surface roughness varied sufficiently to provide information about the effects under investigation.

For data from the Gulf of Mexico, the 1200 Z radiosonde data from Tampa, Florida was used to provide information about the temperature and water vapor profiles. Sea surface temperature was taken from ship reports in the vicinity and was about 28°C. Table 5.1 gives the pressure versus temperature and relative humidity values obtained from the sounding. The relative humidity values have been converted to absolute humidity and they are also listed in the table. Figure 5.1 gives the absorption versus height curve of the sounding and it lies between the hot and standard profiles and the hot and wet profiles.

For data from Flight #6, there were no close radiosonde observations. From looking at the closest stations nearest to the observations; Medford, Oregon, which was slightly north and inland, and Oakland, California,

Table 5.1 Tampa, Florida, 1200 Z sounding (6 June 1967)

Press(mb)	Temp(°K)	Rel Hum(%)	Abs Hum(g/m^3)
1013.25	296.67	86	15.65
980	294.76	70	12.32
950	294.16	62	10.58
900	291.16	64	9.13
850	288.16	66	5.60
800	282.16	39	3.36
750	279.91	43	3.19
700	277.66	47	2.35
600	270.56	44	1.11
500	262.16	30	0.31
400	250.16	16	0.07
300	234.46	15	0.01
200	221.86	10	0.00
100	205.46	05	0.00
5	236.00	05	

which was several hundred miles to the south, it appears that the temperature and relative humidity profiles were very close to the standard and wet atmosphere used previously. Thus, the results from this profile were used in comparison to the observed data. Sea surface temperatures were near 10°C near the coast, based on ship reports.

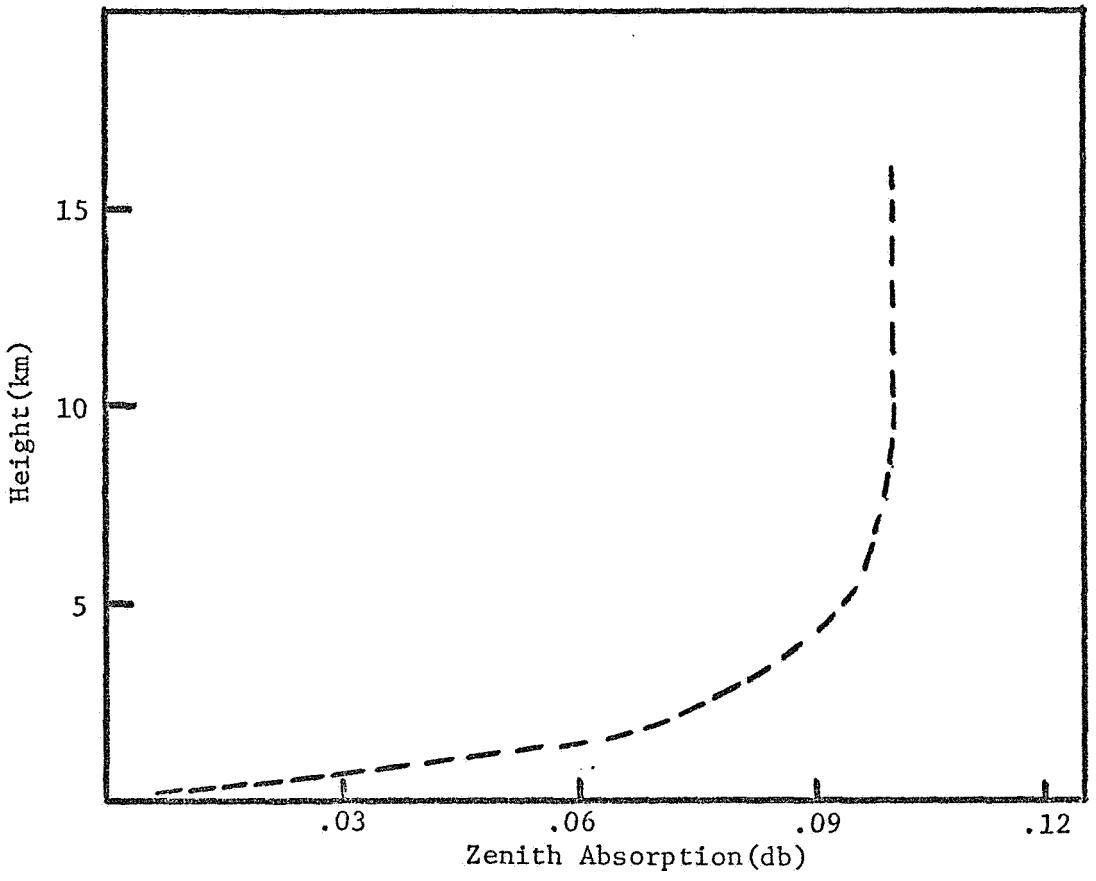

Fig. 5.1 Absorption versus height for Tampa, Florida.

5.3 Data analysis

The observed data have been analyzed and plotted in the following manner. First, the average of five consecutive scans have been averaged for selected angles across the scan to provide a representative cross-section. These five scans represent 8 secs of flight time and were picked to provide a representative average value, yet short enough so that surface features could be considered uniform. The standard deviation has also been plotted to give an indication of the variability of the data. Along with the mean curves described above, the middle scan of the series has also been plotted to show what the actual observed data looks like. The comparison between theory and observation is made between the mean values and the theory.

The data from the flights have been divided into the following categories for analysis:

1. Surface wind speed less than 6 kts, surface smooth to slightly rough.
2. Surface wind speed from 7 to 10 kts, surface rough but no whitecaps are present.
3. Surface wind speed from 11 to 20 kts, surface rough with whitecaps present.

5.4 Light surface wind speeds

Nordberg et al. (1968), measured the brightness temperatures from the Salton Sea on 7 June 1968 when portions of the sea were very smooth and very rough. The curve plotted in Figure 5.2 is the result of their

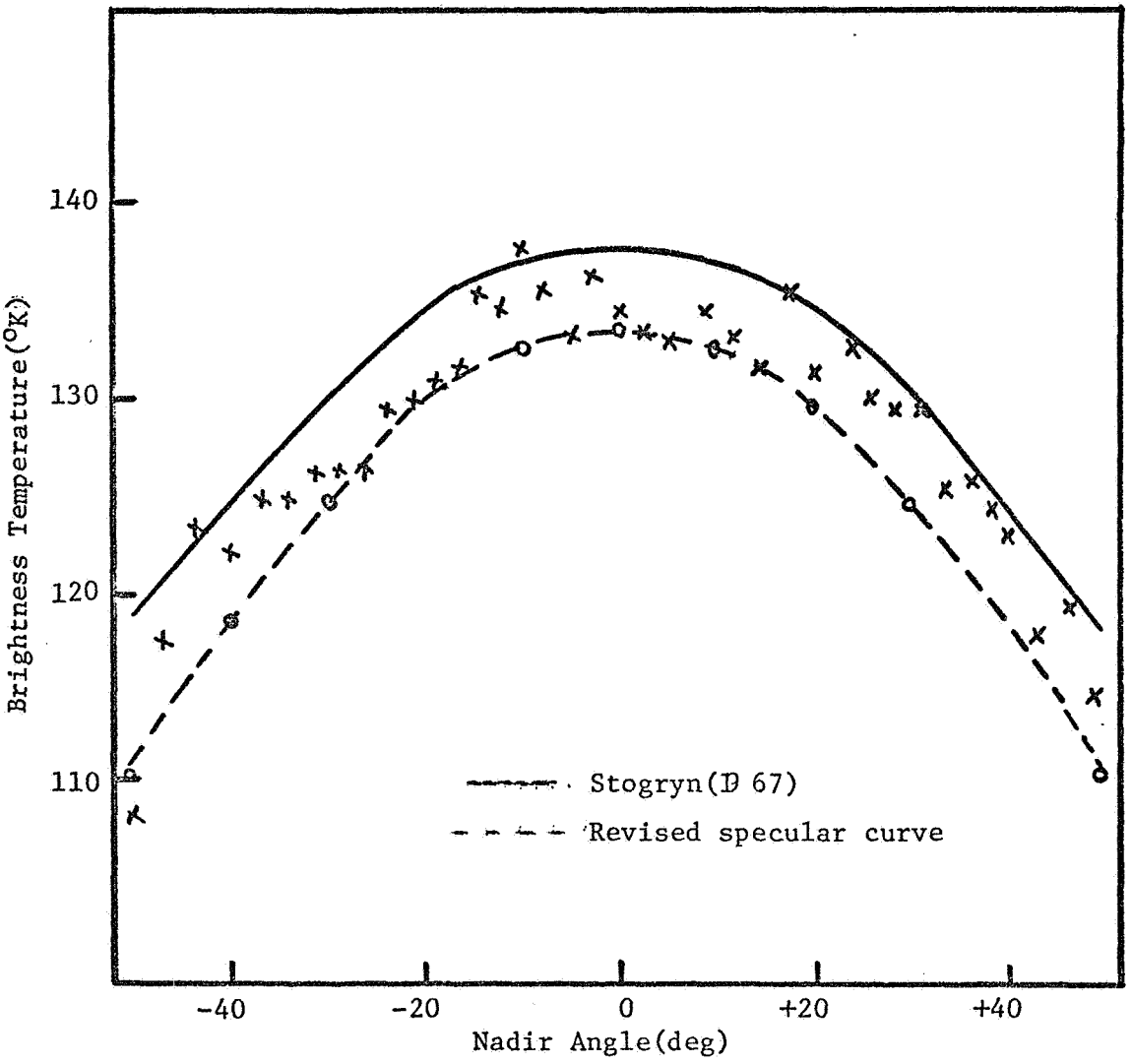

Fig. 5.2 Observed brightness temperatures over the smooth portion of the Salton Sea(after Nordberg et al.,1968).

observations over the smooth portions and represent the average of six consecutive scans. Plotted on the same figure is the result of Stogryn's calculations for a height of 1 km. The difference between the curves amounts to 4°K at nadir viewing and 10°K at -50 degrees. I have plotted the expected brightness temperature from a specular surface using the standard temperature and relative humidity profiles and for an observing height of 1.5 km. The agreement is very good and falls within the variability of the data points.

Two cases of light wind speeds were found on Flight 13, and they are plotted in Figures 5.3 and 5.4; along with the theoretical curves obtained from the Tampa data and assuming specular and diffuse surfaces. At nadir viewing, the observed values are approximately 4°K too low, indicating that there is too much water vapor in the Tampa sounding. This difference is not unexpected for the moist conditions over the Gulf of Mexico and can be accounted for by differences in transmissivity of only 0.02. One feature in Figure 5.3 which should be mentioned is the rising temperatures at large viewing angles. These temperature increases are thought to be due to clouds out of the photographs having their high temperatures reflected into the radiometer. Thus, for generally smooth surfaces, the agreement between theory and observation is good, considering the variability in atmospheric observations.

5.5 Surface rough—no whitecaps

Three cases were found in this category in the Flight 13 data; when the surface appeared rough, yet there was no evidence of breaking waves

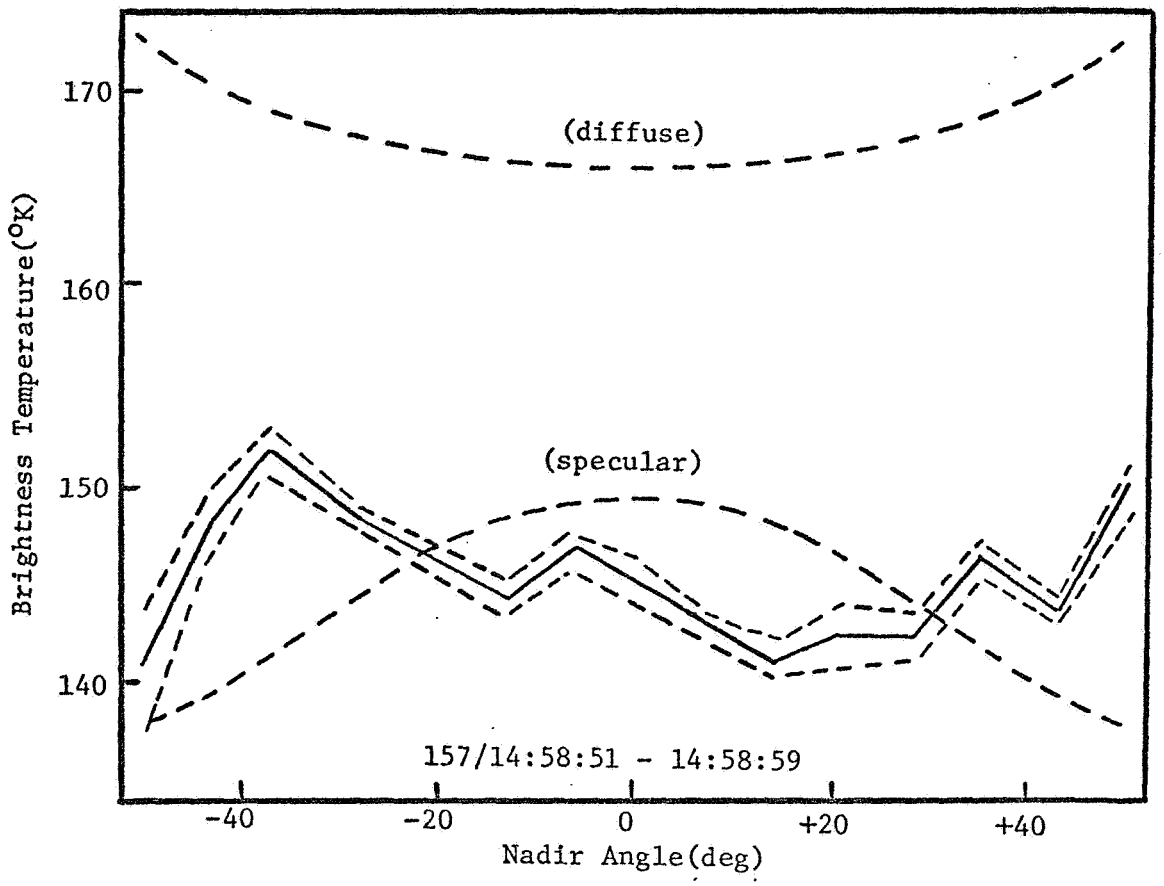

Fig. 5.3a Observed mean brightness temperatures for smooth sea on Flt. 13.

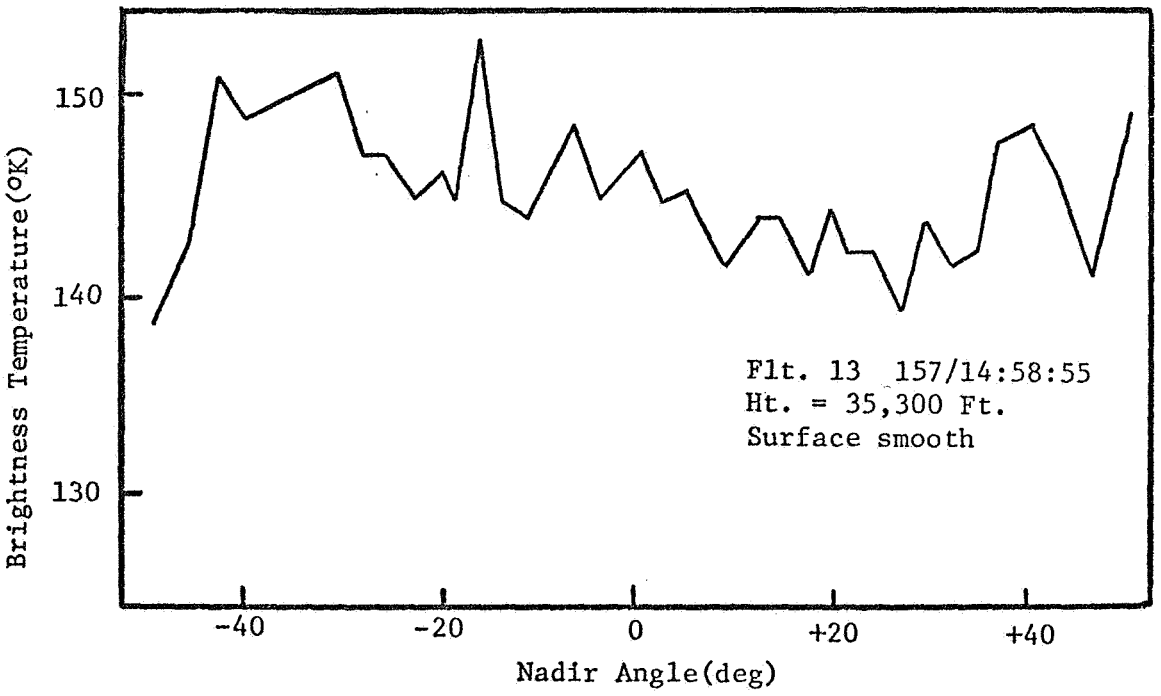

Fig. 5.3b Observed brightness temperatures for smooth sea on Flt. 13.

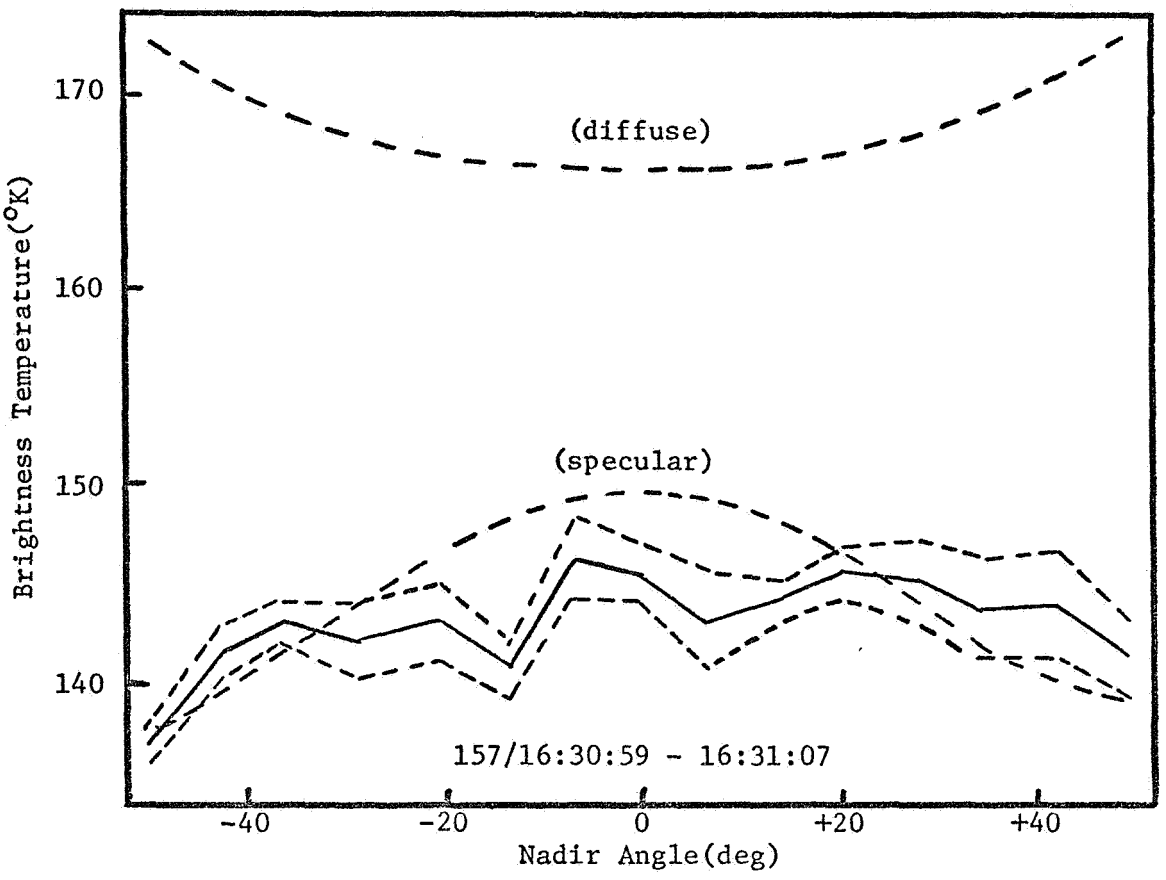

Fig. 5.4a Observed mean brightness temperatures for smooth sea on Flt. 13.

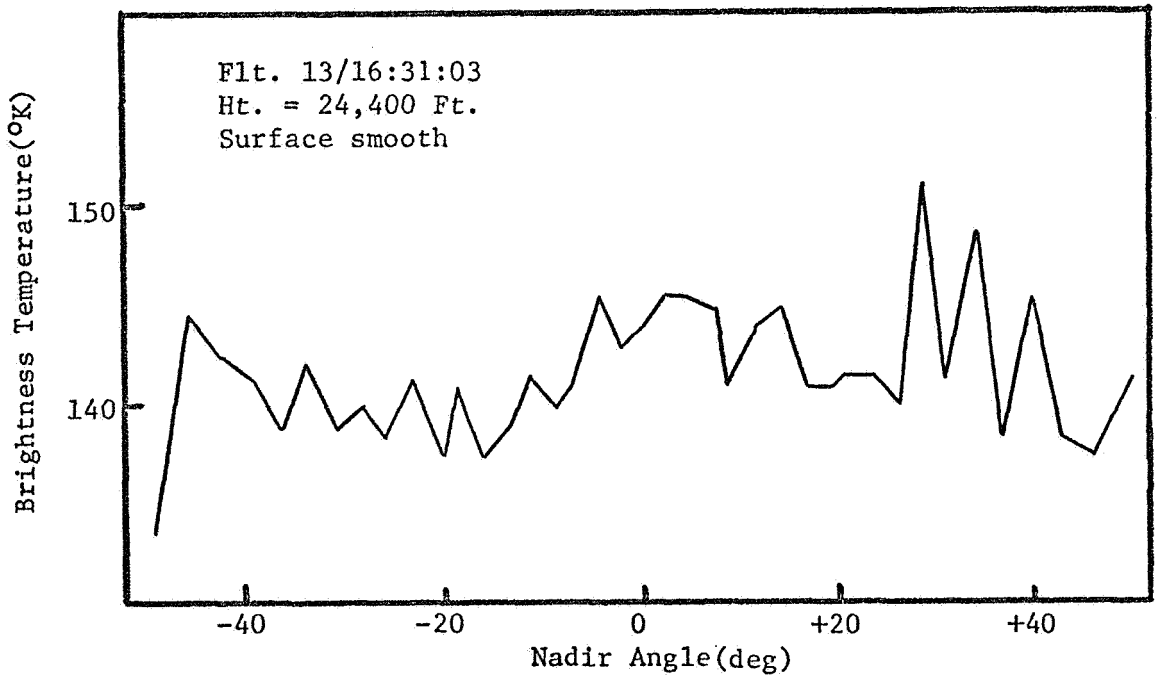

Fig. 5.4b Observed brightness temperatures for smooth sea on Flt. 13.

in the photographs. These curves are shown in Figures 5.5, 5.6, and 5.7. The observed brightness temperatures have increased over those observed under light wind conditions and now lie midway between the curves for the specular and diffuse surfaces. The increase over the specular curve is from 8 to 11°K, which will be 12° to 15°K when corrected for the water vapor in the Tampa sounding. One interesting feature present in all the curves is their general flatness out until viewing angles of ±45 degrees is reached. Stogryn's roughness model, for the wind speed observed, would give the same values as that of the specular curve at nadir viewing angle and a 4°K increase in brightness temperature at ±50 degrees, still not explaining the observed curves.

5.6 Rough water with whitecaps

A total of five cases have been analyzed in this group, three from Flight 13 and two from Flight 6. The cases from Flight 13 will be considered first and are shown in Figures 5.8, 5.9, and 5.10, along with the theoretical curves. In all cases, the curves are 10 to 11°K above the specular surface curve, which will be 14° to 15°K when corrected for the Tampa data, and are generally flat across the scans until ±45 degrees. From the photographs, the percent foam coverage has been estimated at about 1%, which would provide increases in brightness temperature of 1 to 2°K. One interesting feature in the actual data is the appearance of spikes, or values of brightness temperature which are 5 to 10°K higher than the surrounding points. These are thought to be due to the antenna looking at either a patch of foam or a breaking wave at that instant.

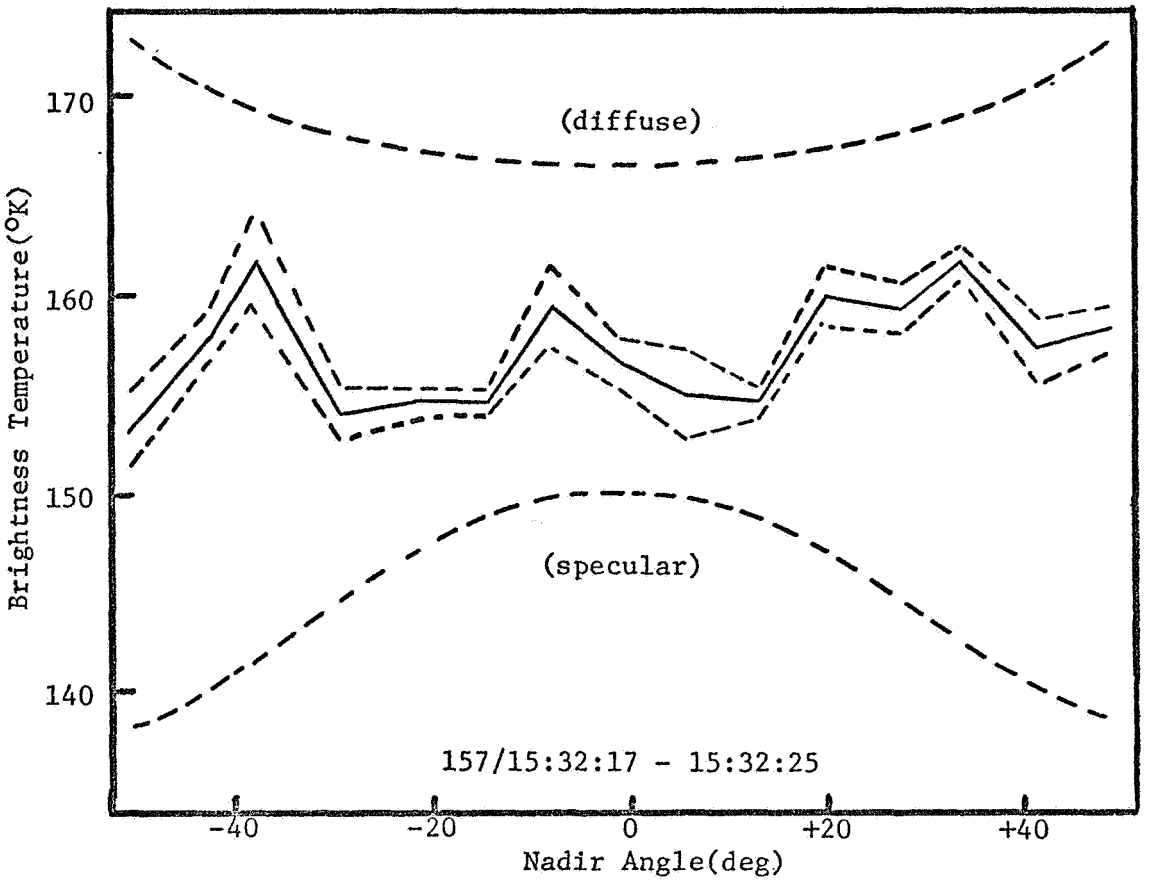

Fig. 5.5a Observed mean brightness temperatures for rough sea on Flt. 13.

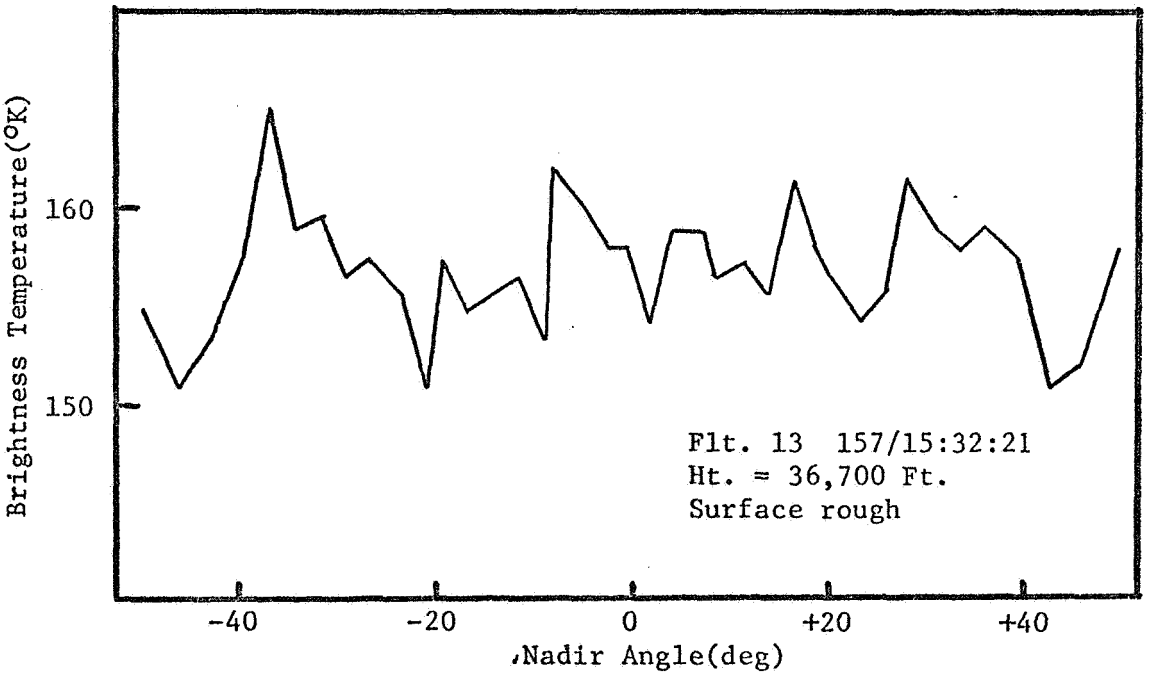

Fig. 5.5b Observed brightness temperatures for rough sea on Flt. 13.

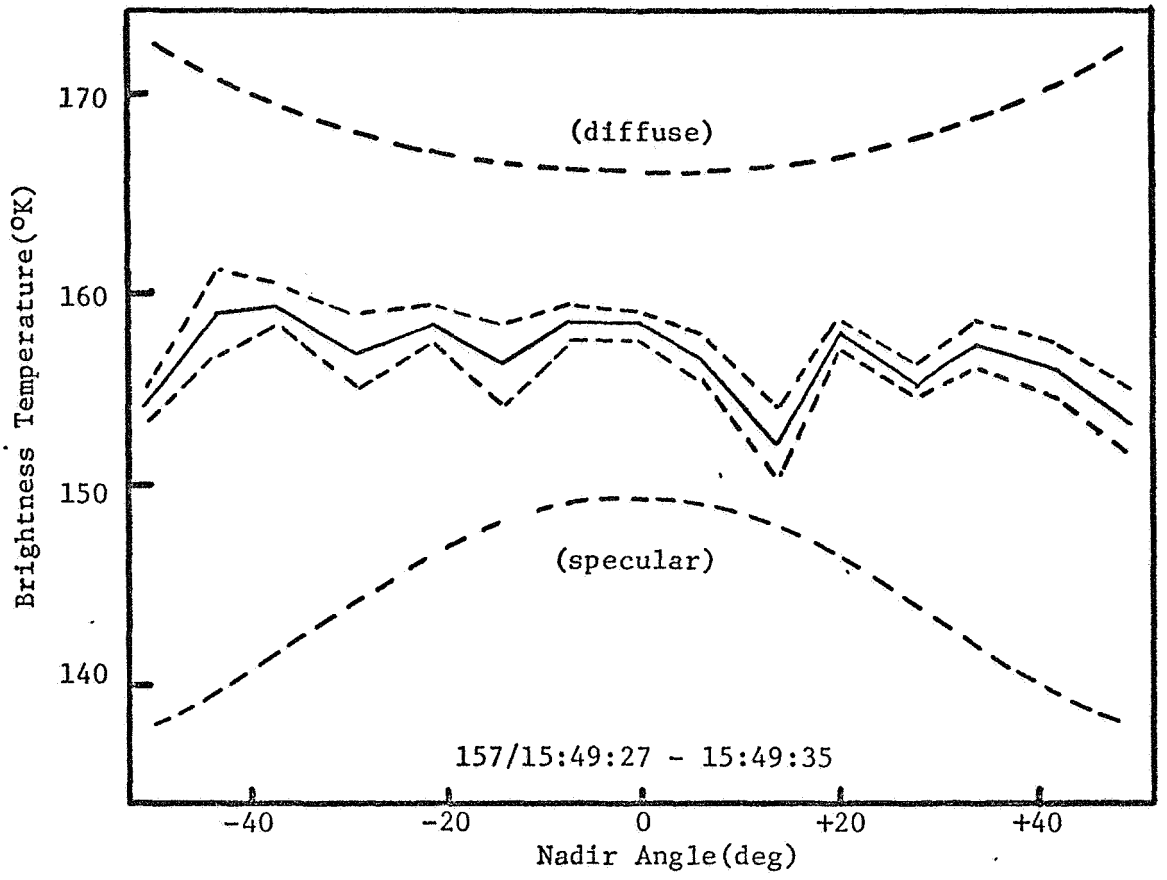

Fig. 5.6a Observed mean brightness temperatures for rough sea on Flt. 13.

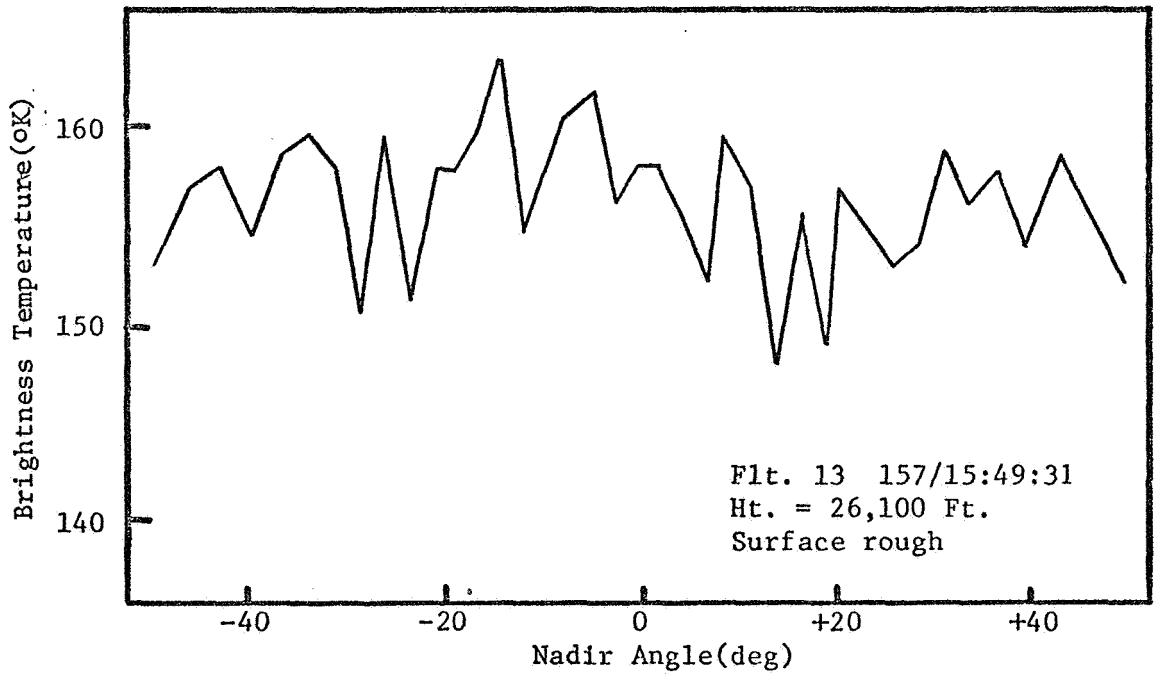

Fig. 5.6b Observed brightness temperatures for rough sea on Flt. 13.

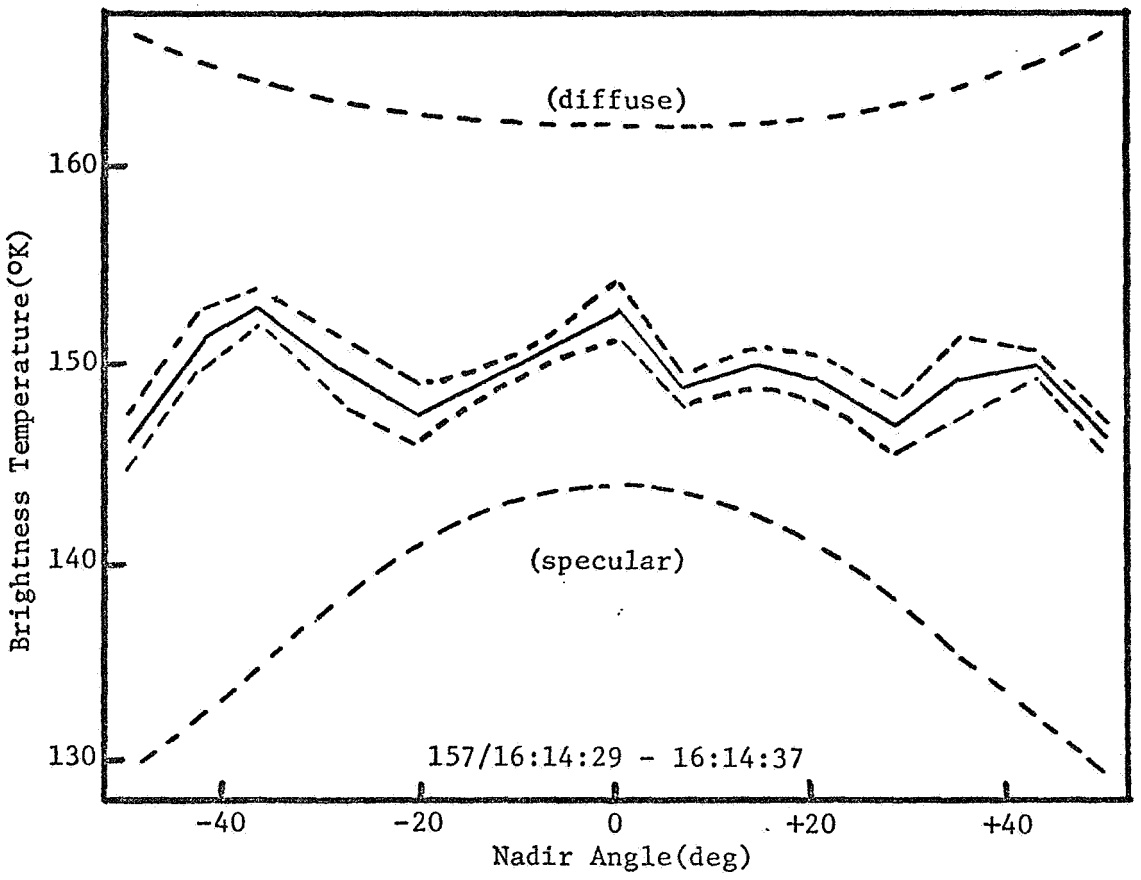

Fig. 5.7a Observed mean brightness temperatures for rough sea on Flt. 13.

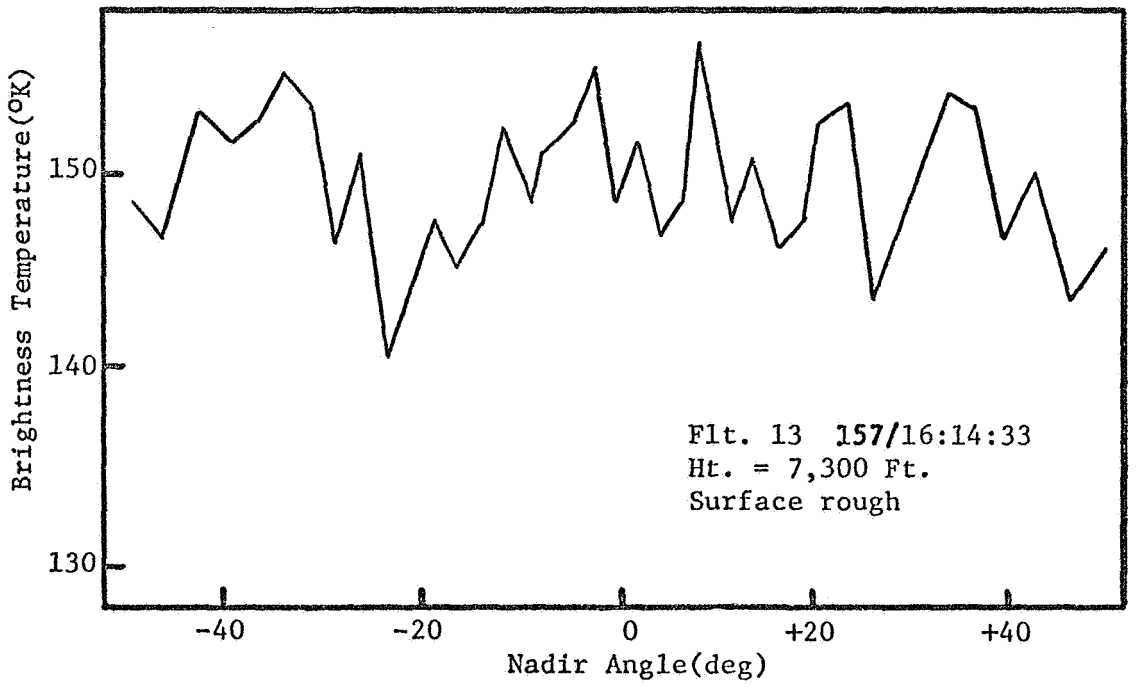

Fig. 5.7b Observed brightness temperatures for rough sea on Flt. 13.

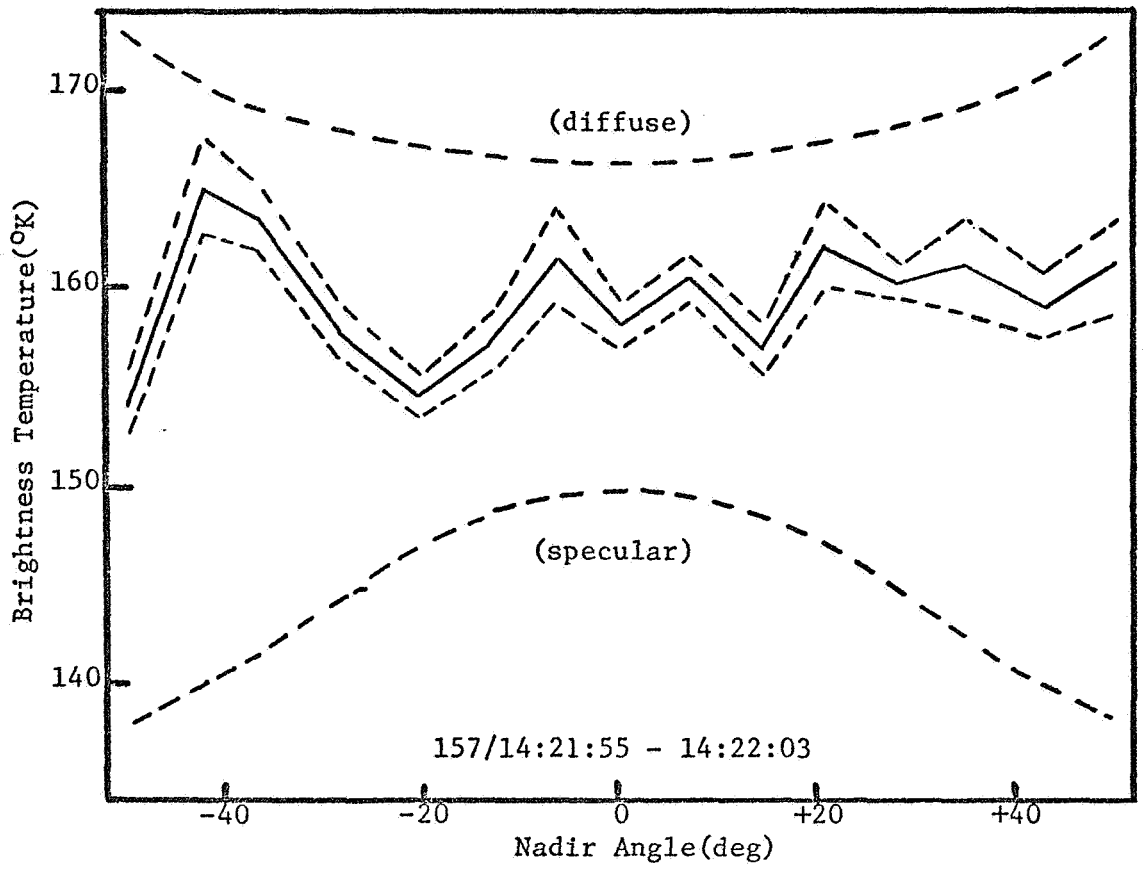

Fig. 5.8a Observed mean brightness temperatures for rough sea with whitecaps on Flt. 13.

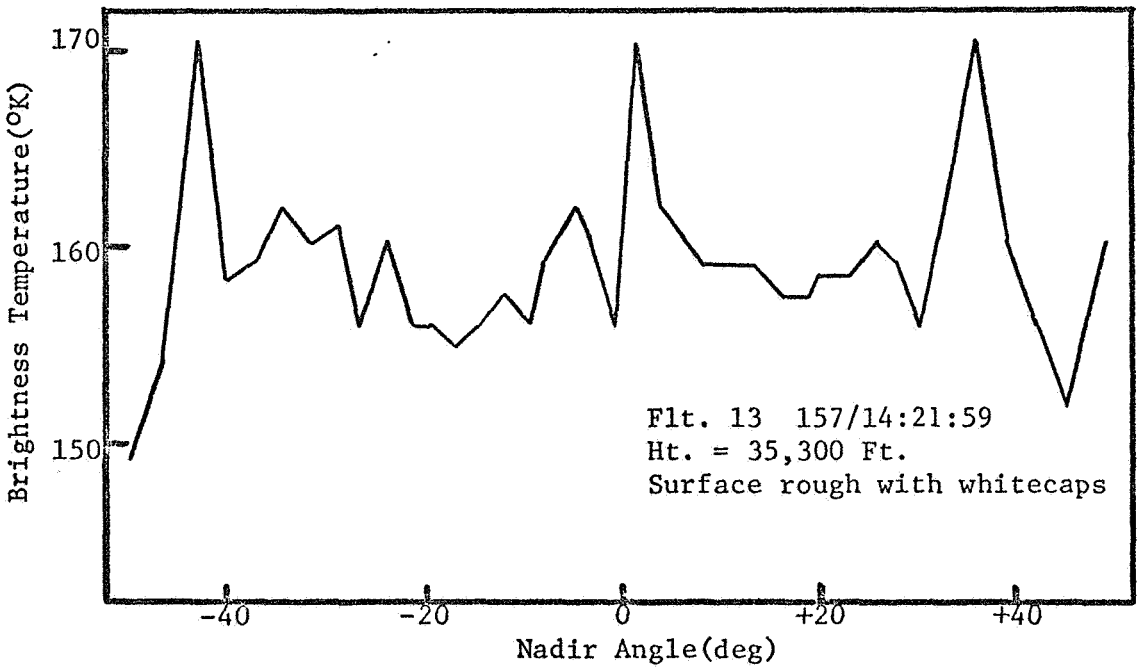

Fig. 5.8b Observed brightness temperatures for rough sea with whitecaps on Flt. 13.

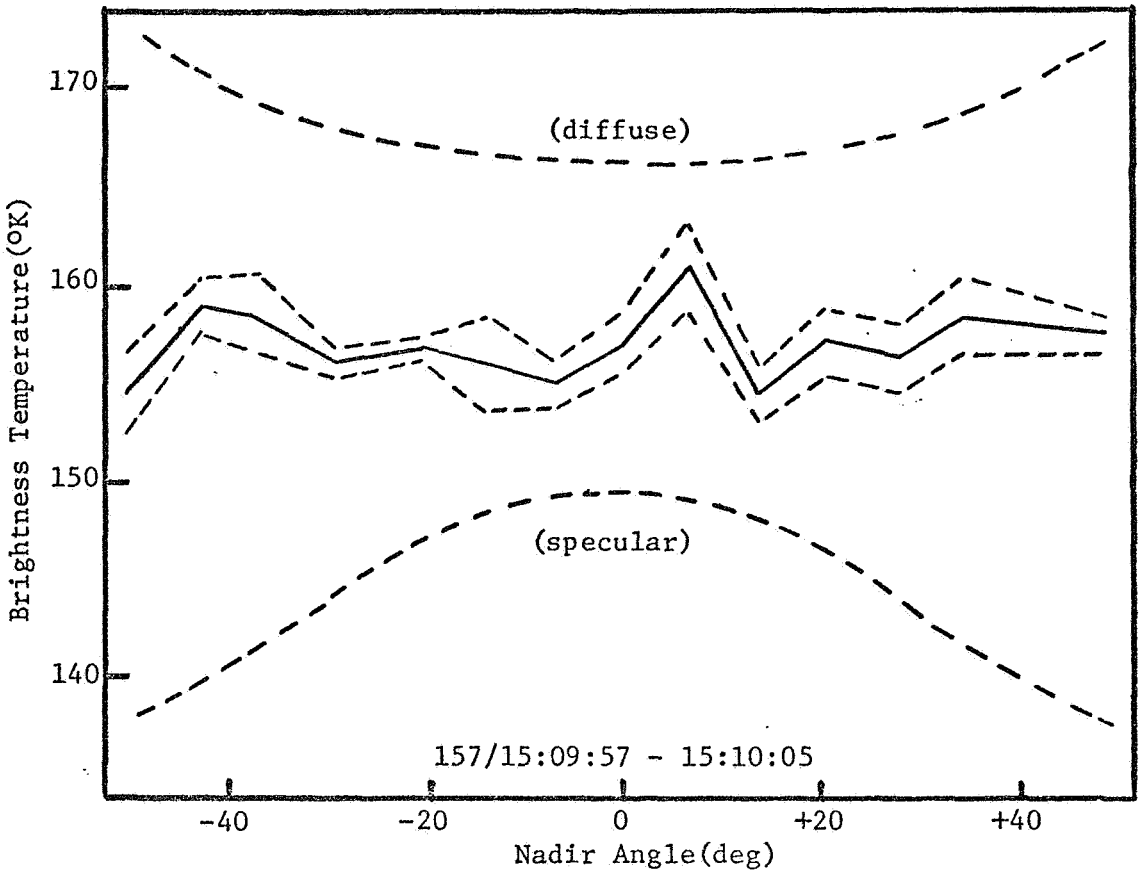

Fig. 5.9a Observed mean brightness temperatures for rough sea with whitecaps on Flt. 13.

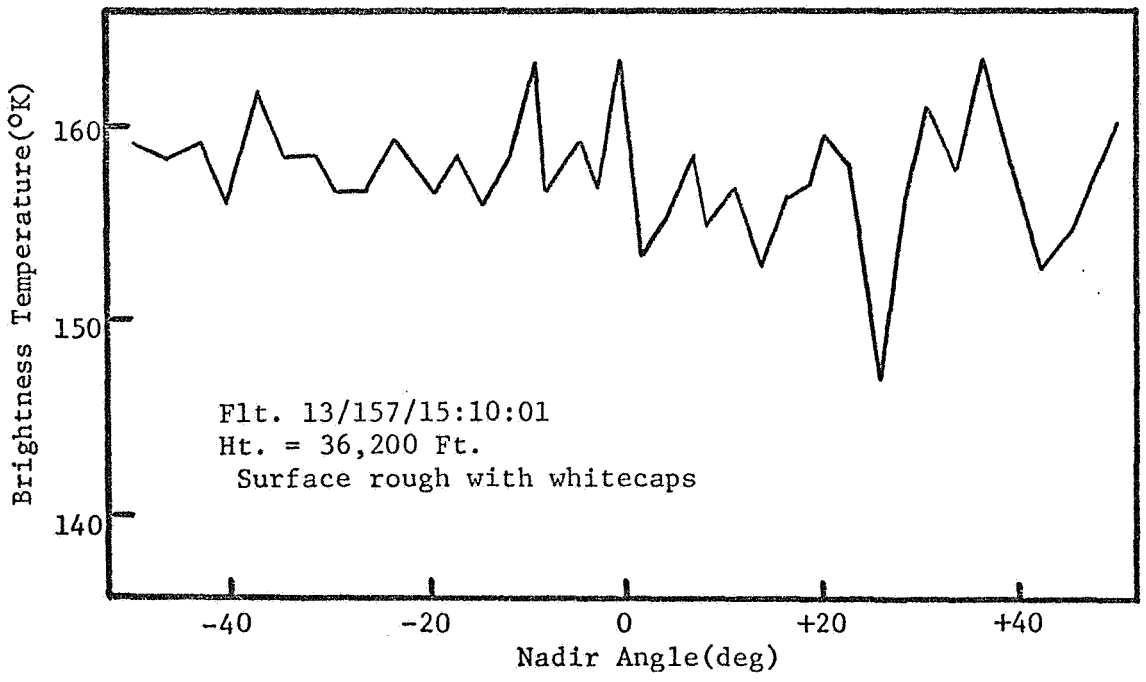

Fig. 5.9b Observed brightness temperatures for rough sea with whitecaps on Flt. 13.

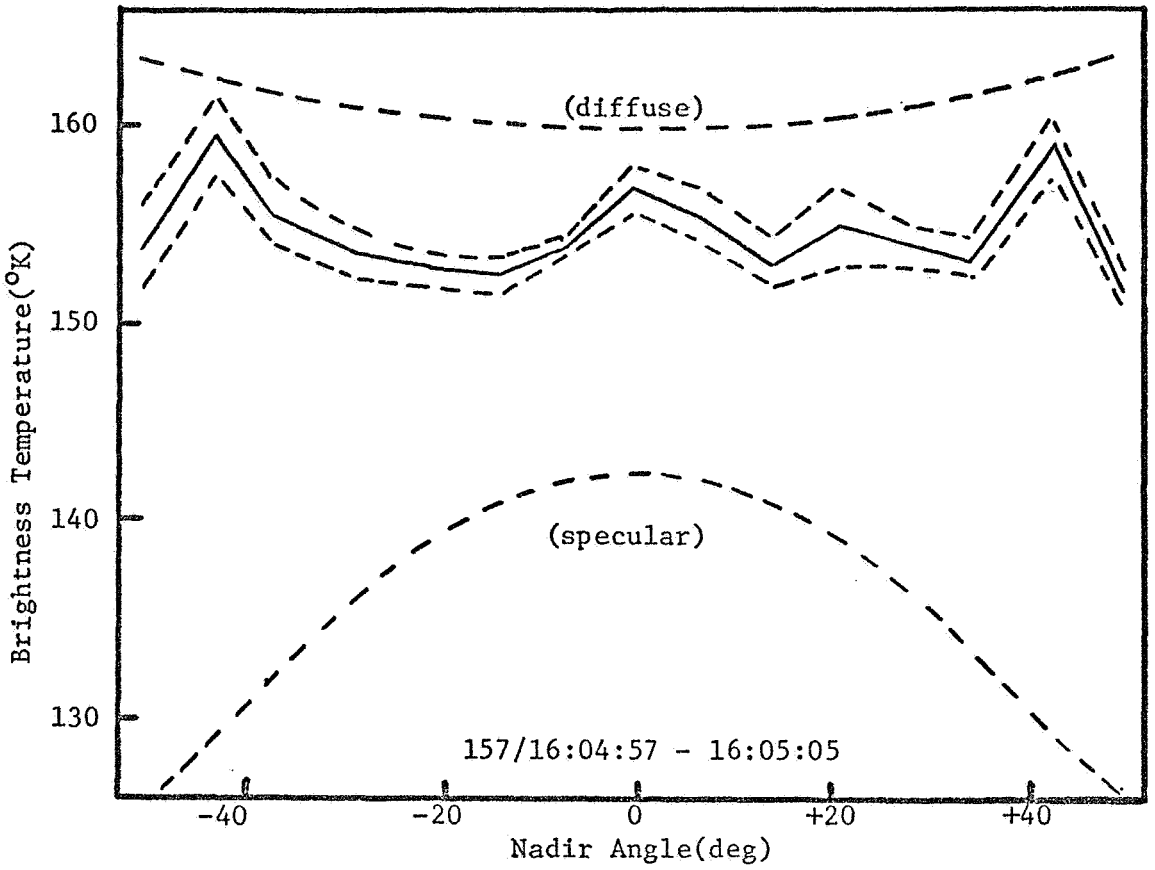

Fig. 5.10a Observed mean brightness temperatures for rough sea with whitecaps on Flt. 13.

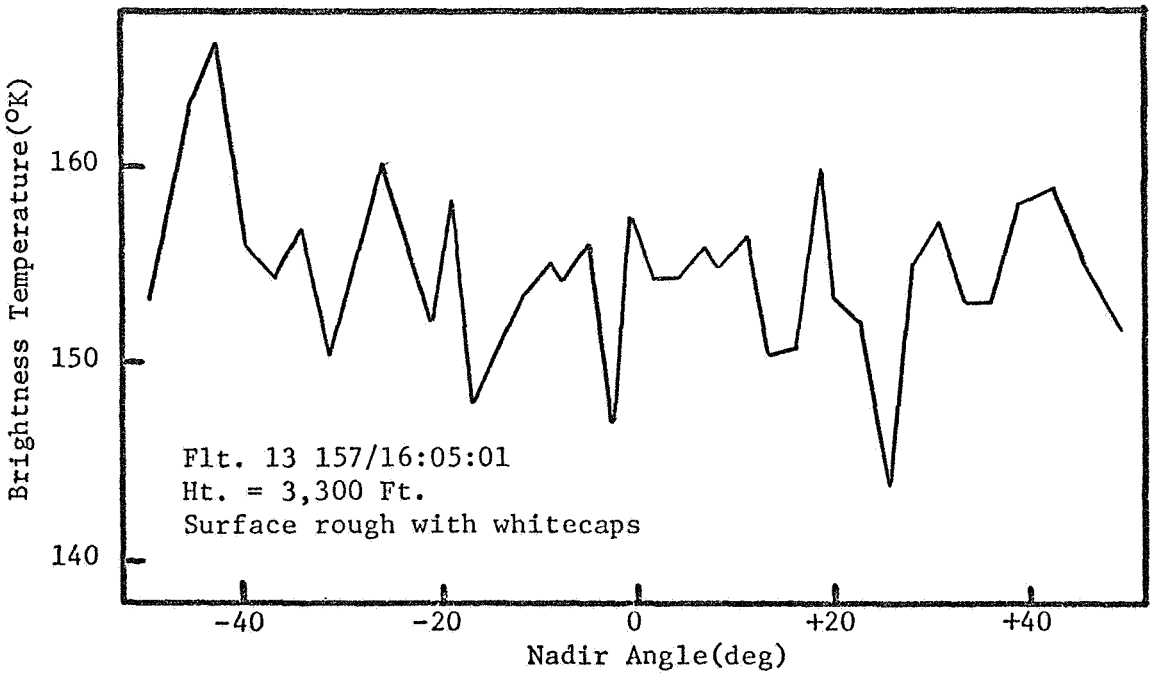

Fig. 5.10b Observed brightness temperatures for rough sea with whitecaps on Flt. 13.

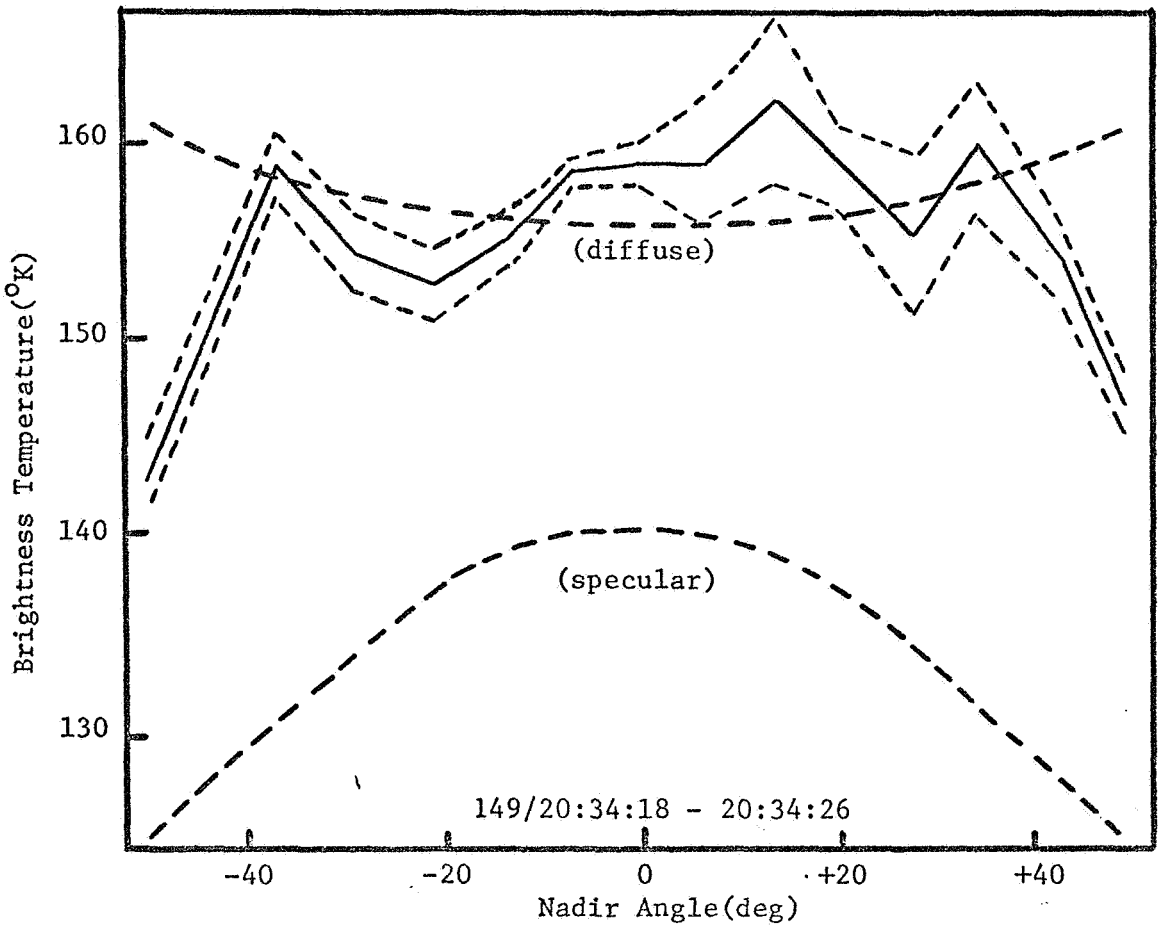

Fig. 5.11a Observed mean brightness temperatures for rough sea with whitecaps on Flt. 6.

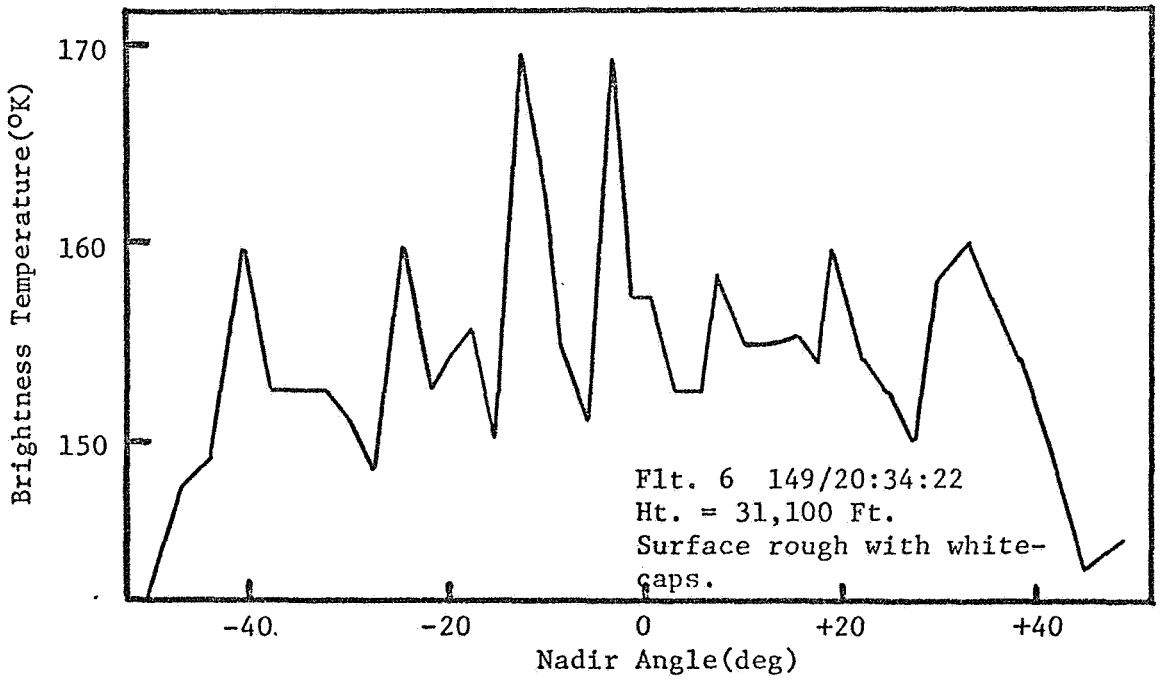

Fig. 5.11b Observed brightness temperatures for rough sea with whitecaps on Flt. 6.

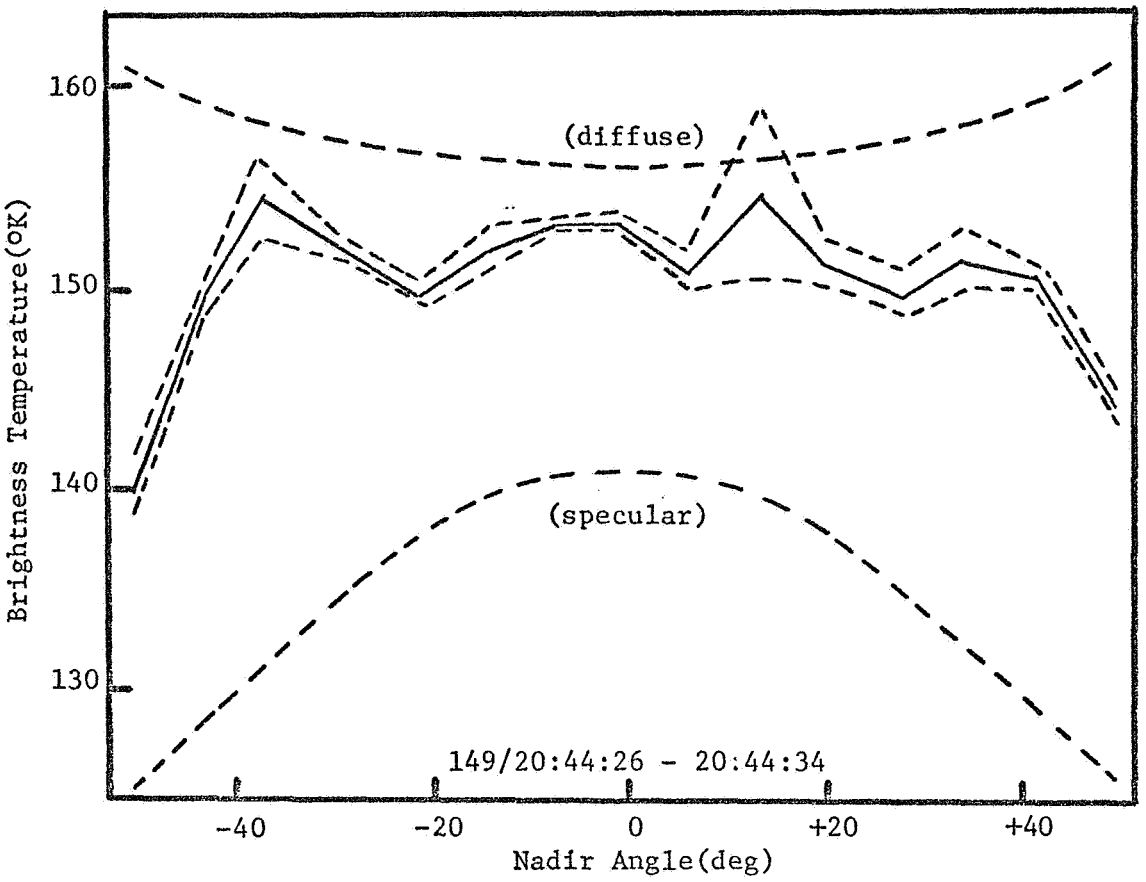

Fig. 5.12a Observed mean brightness temperatures for rough sea with whitecaps on Flt. 6.

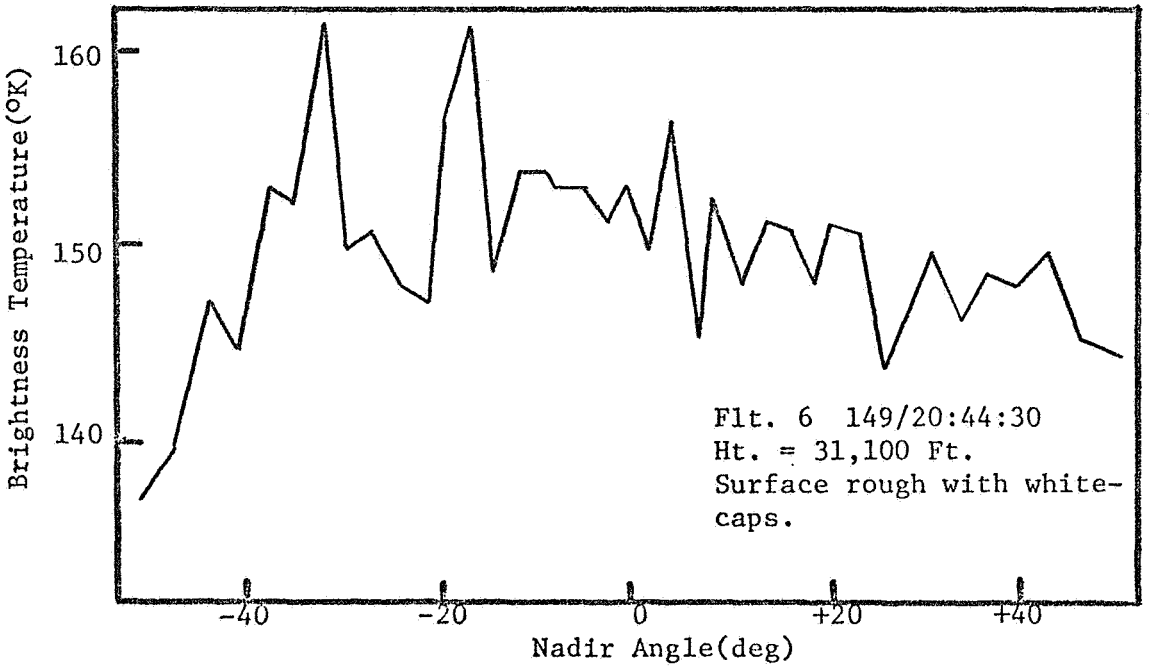

Fig. 5.12b Observed brightness temperatures for rough sea with whitecaps on Flt. 6.

This feature appears to be consistent when foam or whitecaps are present and is one possible way of identifying their presence. A better example will be provided for in the data from Flight 6, to be described below.

The data from Flight 6 was taken off the northern coast of California, just after the coastline was passed. The first case, shown in Figure 5.11, was right after the coastline was passed and there were scattered whitecaps observed in the photographs. The second case, taken about 10 minutes later when there were fewer whitecaps, is shown in Figure 5.12. The increases at nadir viewing are about 18°K for the scattered whitecap case and about 13°K for the case when there were fewer whitecaps. Two other features should be noticed in these curves. The first, in the actual data, is the presence of large spikes; amounting to 14 to 20°K over the surrounding points. The explanation for these spikes is the same as described above. The second feature is the fact that the curves are generally flat out to about ±35 degrees before they start to rapidly drop off. Although the wind speed was only about 15 kts for these cases, the wind speed had been up to 25 kts within the previous 24 hours. This fact, combined with the infinite fetch and the closeness to shore, would provide for greater foam coverage than would be expected from the observed wind speed. Considering these factors, the foam coverage was estimated at 3%, implying a temperature increase due to foam of about 5°K. Thus, foam coverage could partially account for the large temperature increases seen in the data. Stogryn's curves for the estimated roughness, would be generally flat with viewing angle, but have the same value as the specular curve at nadir viewing angle.

5.7 Discussion

The comparison between observed data and theoretical curves have provided the following information:

1. For generally smooth surfaces, the agreement between theory and observation is good, considering the variability in atmospheric observations.
2. As the surface becomes rougher, the brightness temperatures increase at all angles, giving increases up to 15°K at nadir viewing angles.
3. For foam and whitecaps present on the surface, the mean curves yield increases up to 18°K over a specular curve, with point-to-point variations in the actual data of up to 20°K.
4. The curves are generally flat out to ±45 degrees for data over the Gulf of Mexico and to ±35 degrees for data over the Pacific Ocean, before decreasing rapidly.

Thus, two major disagreements have appeared in the comparison between theory and observation and require some explanation. The first is the general increase in brightness temperature seen for rough surfaces, without any breaking waves or foam on the surface. The second is the general flatness of the observed curves out to large viewing angles. The first is the most severe problem and will be discussed first.

Stogryn's theory of scattering from rough surfaces, taking account of the large-scale roughness, predicts no significant change in brightness temperature at nadir viewing for different surface wind speeds; with a specular surface giving a higher brightness temperature than that from a

rough surface. Nordberg et al. (1968), attributes the difference between theory and observation to foam, spray and bubbles. Another explanation is possible, that of small scale roughness on the water surface. That is, the small scale waves ranging from capillary waves on up to several times the observing wavelength. If one neglects shadowing and multiple reflections, the emissivity of the surface shouldn't change because of the assumption that all surfaces will reflect the same total energy, only the distribution of the energy will be different; and the fact that the emissivity is one minus the albedo. Thus, the small scale roughness will act as diffuse reflectors and have the effect of redistributing the energy incident on the surface so that the large sky temperatures at large zenith angles will contribute more to the received brightness temperature. Integrated over a hemisphere, these contributions could become significant and account for the difference between theory and observation.

The flatness of the curves can also be explained by the small scale roughness on the surface. Ruck et al. (1970) have considered backscattering from a composite surface made up of roughness much larger than and much smaller than the observing wavelength. Their results are shown in Figures 5.13 and 5.14. In Figure 5.13, it can be seen that when the slope of the large scale roughness is small, the small scale roughness, which produces the diffuse component, becomes important at angles about 15 degrees from nadir. Figure 5.14 shows that as the slope of the large scale roughness increases, the diffuse component isn't important until angles of 35 degrees from nadir are reached. Now for our situation, the largest incident temperatures occur at large zenith angles. This would mean that

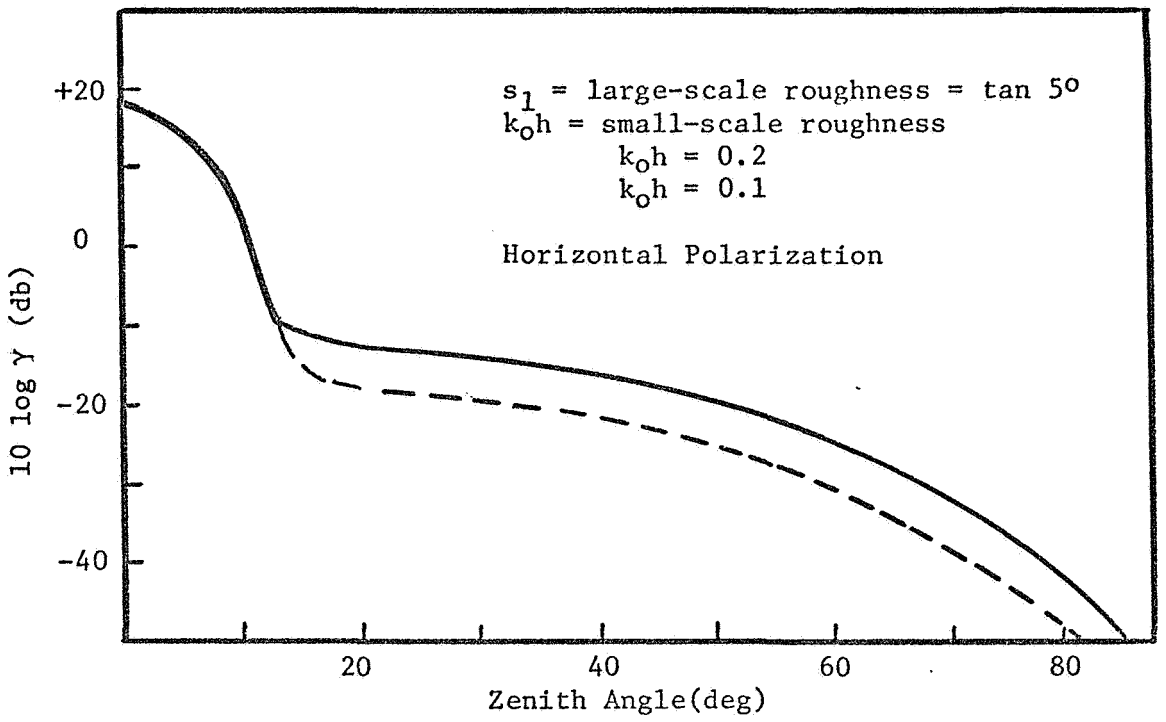

Fig. 5.13 Average backscattering cross-section per unit area for composite surface model of the sea with Gaussian distribution(after Ruck,1970).

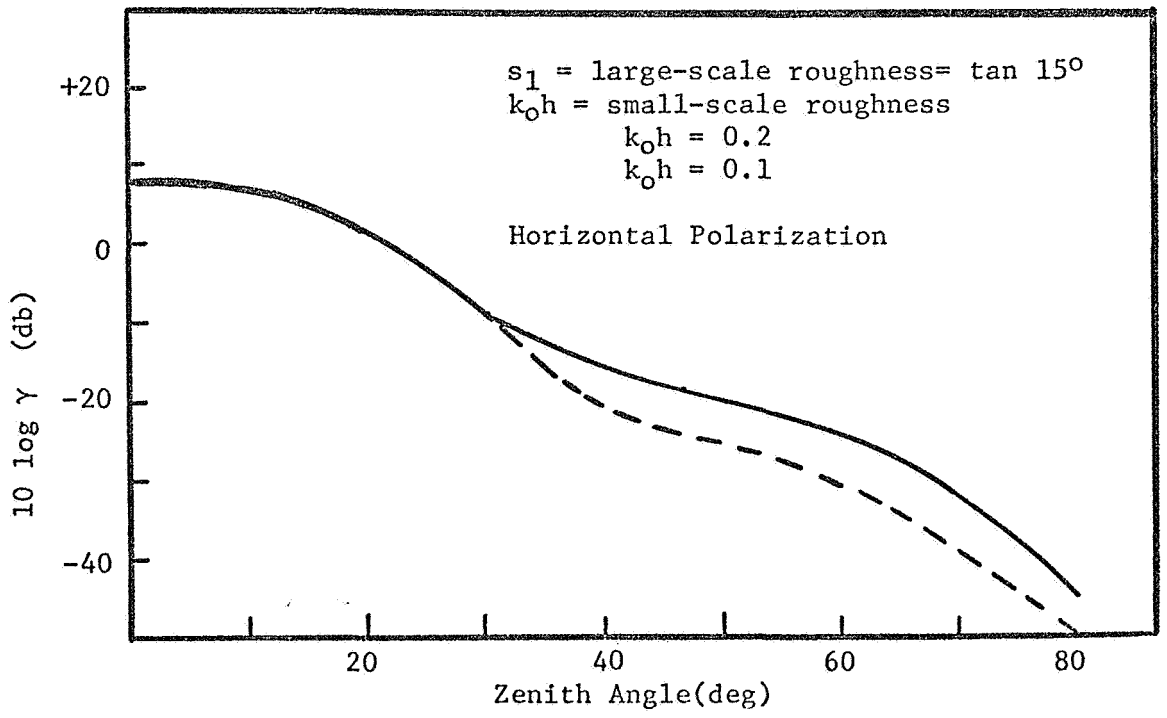

Fig. 5.14 Average backscattering cross-section per unit area for composite surface model of sea with Gaussian distribution(after Ruck, 1970).

these large intensities would be reflected diffusely by the small scale roughness when the slope of the large scale roughness is small. As the slope of the large scale roughness increases, the reflection is more specular and the diffuse component is less important. Thus, with light winds where the mean slope is small, much of the incident radiation will be reflected diffusely by the small scale roughness, giving a generally flat curve with viewing angle. This could explain the observed results over the Gulf of Mexico where the winds were generally light and full sea states were never developed. Over the Pacific Ocean, where the fetch was essentially infinite and the time for development was sufficiently long, the seas were rougher with large mean slopes, meaning that the diffuse component was of less importance and allowing the curves to decrease with angle beyond ±35 degrees.

To determine whether a composite surface would provide closer agreement between theory and observation, a calculation was made using a part specular and part diffuse surface. The calculation was made for the following conditions: 1) a surface temperature of 288.°K; 2) a diffuse reflection coefficient of 0.5656; 3) a standard temperature and relative humidity profile; 4) observer height of 35 km; 5) variable percentages of the surface being diffuse. The results are presented in Figure 5.15 and show the smooth transition from a specular surface, through the composite model and to the diffuse surface. Since most of the rough surface observations were midway between the specular and diffuse curves, one could obtain close agreement to the observed data by assuming a composite surface with about 50% of the surface diffuse. This would give a 7°K

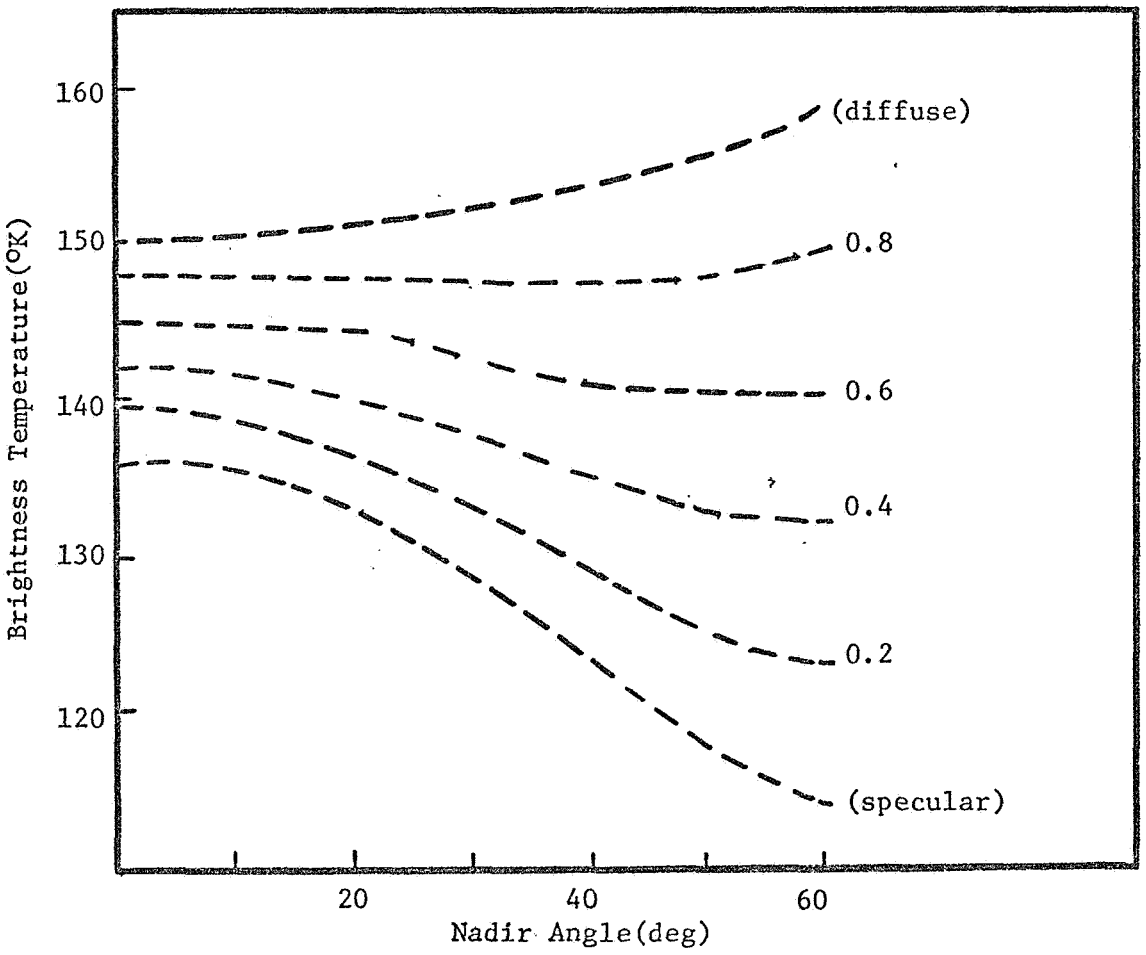

Fig. 5.15 Angular variation of brightness temperature for composite surface model.

increase at nadir viewing angle and a decrease of only 8°K at ±50 degrees. If large scale roughness were included, the decrease at large viewing angles would be even less, making the curves generally flat with angle in agreement with observations. By giving an angular dependence to the diffuse component, making it only effective for radiation incident for specific angles, in agreement with backscattering results; one could possibly account for the flatness to ±45 degrees observed over the Gulf of Mexico and to ±35 degrees for the Pacific Ocean data.

Thus, to obtain better agreement between theory and observation, it is essential that small scale roughness be included in the theory of scattering. The best agreement should come from a composite surface made up of roughness smaller than, the same order as, and much larger than the observing wavelength.

CHAPTER 6

SUMMARY AND RECOMMENDATIONS

The preceding chapters have considered various facets of the problem of downward viewing radiometric observations over the ocean. Both atmospheric and surface effects have been discussed and comparisons have been made between theory and observations, using real atmospheric profiles and surface data as much as possible.

6.1 Summary

It has been found that there is good agreement between theory and observations for generally smooth surfaces, but as the surface becomes rougher, the agreement disappears, amounting up to 20°K for very rough surfaces. One possible explanation for the observed temperature increases, that due to foam, will provide increases that are insufficient to account for the observed brightness temperatures.

Thus, there are two main areas of disagreement between current theory and observation. One is the increase in brightness temperature without the presence of foam or whitecaps and the other is the flatness of the observed data out to large viewing angles. Both of these discrepancies can be qualitatively explained by the presence of small-scale roughness on the surface, which has yet to be accounted for in theory. Increases of up to 15°K might be obtained by including small scale roughness, based on what

has been observed from this study and what can be expected from a diffuse surface model. In addition to the small-scale roughness contribution, the temperature increase due to foam must be added, giving the increases necessary to bring observed data into agreement with the theory.

6.2 Recommendations

There is still work to be done before passive microwave techniques can be used to obtain information about the character of the sea surface and the atmosphere above it. Based on the information obtained in this study, the following recommendations are made with regard to further study.

1. The effect of small-scale roughness should be taken into account in any scattering theory of the surface. The best model would be a composite surface, taking into account roughness smaller than, the same order as, and much larger than the observing wavelength.
2. All future observations should be taken with corresponding atmospheric and surface characteristics included. Without these measurements, only qualitative remarks can be made about the effect of any of the variables.
3. Flights shown should be flown over the same surface at various orientations to see what effect this will have. There is the possibility that this could provide some information about wave orientation, although the variability in the data might overwhelm the effect.

4. Flights should be made from sufficient height to obtain a representative sample of the sea surface, since ocean waves extend from capillary waves on up to waves several hundred feet long.
5. Instruments designed for other frequencies should be used to possibly eliminate the effect of small-scale roughness. A wavelength region can possibly be found so that a surface model using large scale roughness theory would be sufficient to explain the observations, yet provide useful information about the character of the sea surface or the water vapor content of the atmosphere.
6. A detailed study of sea foam and whitecaps should be made with regard to determining the mixture ratio R and the depth of foam over various portions of the ocean surface.

Passive microwave techniques offer a unique tool for understanding and providing information about the atmosphere and the ocean surface. With sufficient effort, understanding will come and passive microwave techniques will become another useful instrument in man's search for knowledge of the world about him.

REFERENCES

Aukland, J. C., P. J. Caruso, W. H. Conway, R. G. Groshans, Remote sensing of the sea conditions with microwave radiometer systems, Proc. 6th Inter. Symp. Remote Sensing of Environ., Ann Arbor, Michigan, 1969.

Aukland, J. C., W. H. Conway, N. K. Sanders, Detection of oil slick pollution on water surfaces with microwave radiometer systems, Proc. 6th Inter. Symp. Remote Sensing of Environ., Ann Arbor, Michigan, 1969.

Blanchard, D. C., The electrification of the atmosphere by particles from bubbles in the sea, Progr. Oceanog., 1, 71, 1963.

Catoe, C., W. Nordberg, P. Thaddeus, G. Ling, Preliminary results from aircraft flight test of an electrically scanning microwave radiometer, Tech. Rept. X-662-67-352, Goddard Space Flight Center, Greenbelt, Maryland, 1967.

Cox, C. S. and W. H. Munk, Measurements of the roughness of the sea surface from photographs of the sun's glitter, J. Opt. Soc. Am., 44, 838-850, November, 1954a.

Cox, C. S. and W. H. Munk, Statistics of the sea surface derived from sun glitter, J. Marine Res., 13, 198-227, February, 1954b.

Droppleman, J. D., Apparent microwave emissivity of sea foam, J. Geo. Res., 75, 696-698, January, 1970.

Garrett, W. D. The influence of surface-active material on the properties of air bubbles at the air/sea interface, Naval Research Laboratory Report 6545, May, 1967.

Gaut, N. E., Studies of atmospheric water vapor by means of passive microwave techniques, Tech. Rept. 467, Massachusetts Institute of Technology, Research Laboratory of Electronics, Cambridge, Massachusetts, 1968.

Kraus, J. D., Radio Astronomy, McGraw-Hill, New York, 1966.

Kreiss, W. T., Meteorological observations with passive microwave system, 198pp., Boeing Scientific Research Laboratories Document, DI-82-0692, Boeing Aircraft Company, Seattle, Washington, February, 1968.

Lane, J. A., and J. A. Saxton, Dielectric dispersion in pure polar liquids at very high radio frequencies, Proc. Roy. Soc. London, A, 213, 400-408, 1952.

Miyake, Y., and T. Abe, A study on the foaming ability of sea water,Part I, J. Marine Res., 7, 67-73, 1948.

Monahan, E. C., Fresh water whitecaps, J. Atms. Sci., 26, 1026-1029, September, 1969.

Monahan, E. C., and C. R. Seitlow, Laboratory comparisons of fresh-water and salt-water whitecaps, J. Geo. Res., 74, 6961-6966, December, 1969.

Munk, W. H., A critical wind speed for air-sea boundary processes, J. Marine Res., 6,(3), p. 203, 1947.

Nordberg, W.,J. Conaway, P. Thaddeus, Microwave observations of sea state from aircraft, Tech. Rept. X-620-68-414, Goddard Space Flight Center, Greenbelt, Maryland, 1968.

Odelevskii, V. I., J. Tech. Phys., Moscow, 21, 667, 1951.

Paris, J. F., Microwave radiometry and it's application to marine meteorology and oc-anography, Ref. 69-1T, Dept. Oceano., Texas A & M Univ., College Station, Texas, 1969.

Peake, W. H., The microwave radiometer as a remote sensing instrument, Report 1903-8, The Ohio State University Electroscience Laboratory, Columbus, Ohio, 1969.

Ruck, G. T., D. E. Barrick, W. D. Stuart, C. K. Krichbaum, Radar Cross-section Handbuck, II, Plenum Press, New York, 1970.

Sirounian, V., Effect of temperature, angle of observation, salinity and thin ice on the microwave emission of water, J. Geo. Res., 73, July, 1968.

Stogryn, A., The apparent temperature of the sea at microwave frequencies, IEEE Transactions on Antennas and Propagation, AP-15, 278-286, March, 1967.

Tobin, M. S., Support data for Convair 990 meteorological flight II, May 5-June 8,1967, Tech. Rept. X-622-67-450, Goddard Space Flight Center, Greenbelt, Maryland, 1967.

Williams, G. F., Microwave radiometry of the ocean and the possibility of marine wind velocity determination from satellite observations, J. Geophys. Res., 74(18), 4591, 1969.